Surface plasmon polaritons: physics and applications

2012 J. Phys. D: Appl. Phys. 45 113001

(http://iopscience.iop.org/0022-3727/45/11/113001)

IOP PUBLISHING JOURNAL OF PHYSICS D: APPLIED PHYSICS

J. Phys. D: Appl. Phys. **45** (2012) 113001 (19pp) doi:10.1088/0022-3727/45/11/113001

TOPICAL REVIEW

Surface plasmon polaritons: physics and applications

Junxi Zhang, Lide Zhang and Wei Xu

Institute of Solid State Physics, Key Laboratory of Materials Physics, Chinese Academy of Sciences, and Anhui Key Laboratory of Nanomaterials and Nanotechnology, Hefei 230031, People's Republic of China

E-mail: jxzhang@issp.ac.cn and ldzhang@issp.ac.cn

Received 28 October 2011, in final form 31 December 2011
Published 27 February 2012
Online at stacks.iop.org/JPhysD/45/113001

Abstract

Surface plasmon polaritons (SPPs) are electromagnetic excitations existing at the interface between a metal and a dielectric material. Remarkable progress has been made in the field of SPPs in recent years. Control and manipulation of light using SPPs on the nanometre scale exhibit significant advantages in nanophotonics devices with very small elements, and SPPs open a promising way in areas involving environment, energy, biology and medicine. This paper presents an overview of current research activities on SPPs, including fundamental physics and applications. We first discuss the excitation of SPPs based on the SPP dispersion relation, coupling to SPPs by momentum matching between photons and SPPs, and propagation behaviour of SPPs. Based on the physical mechanism and the peculiar properties of SPPs, we demonstrate the major applications of SPPs, such as waveguides, sources, near-field optics, surface-enhanced Raman spectroscopy, data storage, solar cells, chemical sensors and biosensors.

(Some figures may appear in colour only in the online journal)

1. Introduction

With the rapid development of optical techniques, data transmission systems require highly increasing integration of photonic devices. It is estimated that the data transmission rates will reach 10 Tbit s^{-1} by decreasing the element size of the photonic devices to the nanometre scale; in this case, the data storage density will be as high as 1 Tbit $inch^{-2}$. However, it is very difficult for conventional photonic devices to reduce the element sizes to the nanometre scale because of Abbe's diffraction limit to about one-half of the optical wavelength. Excitation of surface plasmon polaritons (SPPs) can overcome the diffraction limit and offer a promising approach to control and manipulation propagation and dispersion of light on the nanometre scale. SPP is an electromagnetic excitation existing at the interface between a metal and a dielectric material; furthermore, the resonant interaction between the SPP and the electromagnetic radiation at metallic interfaces results in a remarkably enhanced optical near-field.

SPPs were first observed by Wood in 1902; he found unexplained features in optical reflection measurements on metallic gratings [1]. Then, Maxwell Garnett observed bright colours in metal-doped glasses [2], and Mie proposed the theory of light scattering by spherical particles in 1908 [3]. Pines theoretically described the characteristic energy losses experienced by fast electrons travelling through metals in 1956 [4], and he attributed these losses to collective oscillations of free electrons in the metal, and called these oscillations 'plasmons'. In the same year, Fano introduced the term 'polariton' for the coupled oscillation of bound electrons and light inside transparent media [5]. Thereafter, Ritchie investigated electron energy losses in thin films and performed the first theoretical description of surface plasmons [6]. It was found that plasmon modes could exist near the surface of metals; then, he described the anomalous behaviour of metal gratings in terms of surface plasmon resonances excited on the gratings [7]. Otto and Kretschmann proposed optical excitation of surface plasmons on metal films [8, 9]. Major

progress was made when the surface plasmon properties of gold and silver nanoparticles were described by Kreibig and Zacharias for the first time [10]. Several years later, Cunningham and co-workers introduced the term surface plasmon polariton (SPP) [11].

In recent years, fundamental research and development of SPP-based structures and devices has received increasing interest due to its peculiar properties and applications in optics, surface-enhanced Raman spectroscopy (SERS), data storage, solar cells, sensors, etc [12]. For instance, a new scanning plasmon near-field microscope with a high lateral resolution of 3 nm ($\lambda/200$) was achieved based on the enhanced near-field between sample and metal tips owing to the resonantly excited extended SPP waves [13]. On the other hand, the magnitude of the near-field enhancement was expected to be 100–200 times as large as the incident electromagnetic radiation and indicated a high detection efficiency in near-field spectroscopy [14]. Five-dimensional (e.g. integration of wavelength, polarization and spatial dimensions) optical recording has been performed by exploiting the unique properties of the longitudinal SPP resonance of gold nanorods [15]. Concretely, the recordings were detected using longitudinal SPP resonance mediated two-photon luminescence, and as a result, a recording disk capacity of 7.2 Tbit and a recording speed of 1 Gbits^{-1} were obtained. SPP-based silver nanoparticles of diameter 40–100 nm can work as a biosensing label, and the detection sensitivity in a DNA hybridization assay is about 60 greater than that achieved using fluorescent labels [16]. Raman signals of adsorbed molecules can be amplified, and using SPP-based silver nanoparticles, the intrinsic Raman enhancement factors are on the order of 10^{14} for single Rhodamine 6G molecules adsorbed on selected nanoparticles [17], which is much larger than the ensemble-averaged values derived from conventional measurements.

This paper reviews physics and applications of SPPs. The main content of this paper consists of several sections: the next section (section 2) discusses some fundamental concepts of SPPs, involving excitation of SPPs, coupling to SPPs and their propagation behaviour. Based on the exploration of physics of SPPs, typical applications of SPPs are demonstrated in section 3, such as optics, SERS, data storage, solar cells, chemical sensors and biosensors. Brief conclusions and remarks on SPPs are given in the final section.

2. Physics of surface plasmon polaritons

2.1. Excitation of surface plasmon polaritons

SPPs are surface electromagnetic waves that propagate along the interface between a metal and a dielectric material, and the surface electromagnetic waves consist of surface charges. First of all, how to excite the surface charges? We consider a p-polarized wave (TM mode, the electric field vector parallel to the incident plane) that reaches a smooth planar interface at an incident angle θ_1 (figure 1). The incident wave has a photon momentum $\hbar k_d$ (where $k_d = 2\pi n_d/\lambda$) in the dielectric with a refractive index n_d. When the wave arrives at the interface, the reflective wave will propagate along the direction with an angle equal to the incident angle, and the photon momentum is conserved. Moreover, the wave in the metal propagates in a new direction with a refractive angle θ_2. The photon momentum is $\hbar k_m$ (where $k_m = 2\pi n_m/\lambda$, n_m is the refractive index of the metal), and the momentum component along the x direction is conserved, i.e. $k_{dx} = k_{mx}$, where $k_{dx} = k_d \sin\theta_1$ and $k_{mx} = k_m \sin\theta_2$, and we have

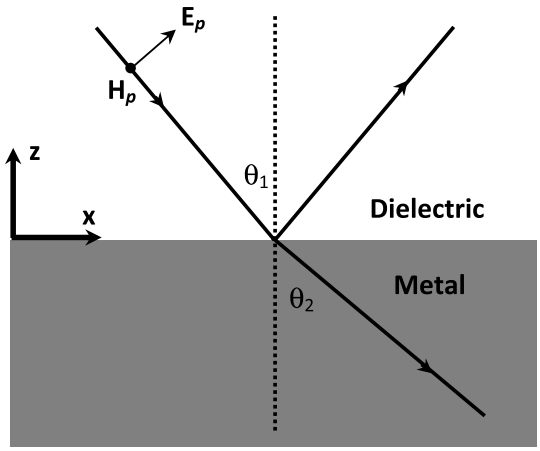

Figure 1. Representation of p-polarized electromagnetic radiation incident upon a planar interface between two media at an angle of incidence θ_1.

$$n_d \sin\theta_1 = n_m \sin\theta_2. \tag{2.1}$$

This relation is called Snell's law. In general, the refractive index of the dielectric n_d is larger than that of the metal n_m (especially noble metal) at the visible wavelength, e.g. considering several wavelengths, for copper $n_m = 0.826$ at 563.5 nm, $n_m = 0.272$ at 619.9 nm; for gold $n_m = 0.608$ at 516.6 nm, $n_m = 0.306$ at 563.6 nm; for silver $n_m = 0.173$ at 400 nm, $n_m = 0.120$ at 563.6 nm [18]. Since $n_d > n_m$ for these wavelengths, the maximum value of θ_2 is 90°, and the incident angle θ_1 is limited. Beyond the limiting angle, the wave cannot propagate in the metal; in this case, the limiting incident angle is called the critical angle θ_c, which is given by

$$\sin\theta_c = \frac{n_m}{n_d}. \tag{2.2}$$

A wave with incident angle beyond θ_c has more momentum along the surface plane than can be supported by the metal. For the p-polarized wave incident on the interface, the oscillating electric field will cause surface charges at the interface between the metal and the dielectric, and the surface charges undergo a collective oscillation. Although the wave is totally reflected at the interface there are oscillating charges which have associated radiation fields penetrating into the metal. They are spatially decaying fields (evanescent fields) in a direction normal to the interface (figure 2). At the critical angle the decay length is infinite but this falls rapidly to the order of the wavelength of light as the angle of incidence increases further. In these cases, the evanescent fields for the incident wave beyond the critical angle are useful for coupling radiation to SPPs.

Since there is no boundary orthogonal to E_x, this component is conserved across the boundary. However, this

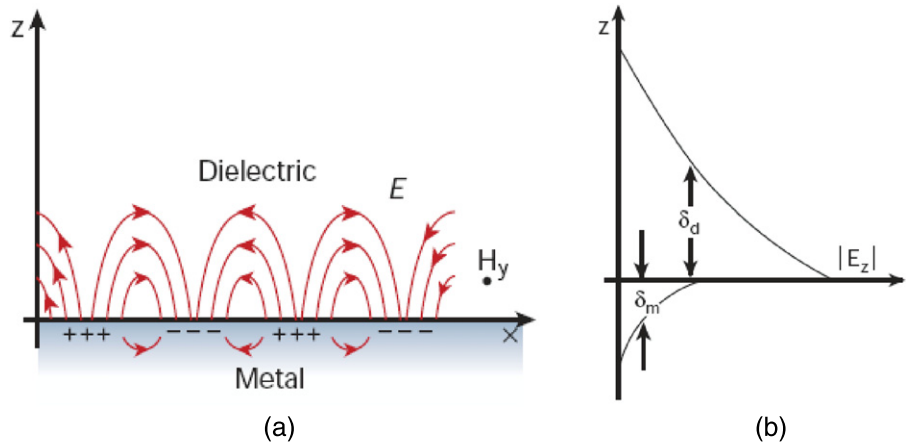

Figure 2. (*a*) Schematic illustration of electromagnetic wave and surface charges at the interface between the metal and the dielectric material, (*b*) the locally electric field component is enhanced near the surface and decay exponentially with distance in a direction normal to the interface.

is not the case for E_z the normal component of $\boldsymbol{E}$; the normal component of $\boldsymbol{D}$, D_z, is continuous (there is no free charge), and E_z is forced to change if ε is changed since $D_z = \varepsilon_\mathrm{d}\varepsilon_0 E_{z\mathrm{d}} = \varepsilon_\mathrm{m}\varepsilon_0 E_{z\mathrm{m}}$. This discontinuity in E_z results in polarization changes at the interface. From these simple considerations it is obvious that while s-polarized incident radiation will not normally cause the creation of charges at a planar interface, p-polarized wave will automatically create time-dependent polarization charges at the interface. Because of the requirement of the normal $\boldsymbol{E}$ fields to create surface charges, we need only consider p-polarized electromagnetic waves. Further, whatever form the surface wave takes it has to satisfy the electromagnetic wave equation in the two media. If the x–y plane is the interface plane, for wave propagation in the x direction only, when $z > 0$, one has [19, 20]

$$E_\mathrm{d} = (E_{x\mathrm{d}}, 0, E_{z\mathrm{d}}) \exp(-k_{z\mathrm{d}} z) \exp[\mathrm{i}(k_x x - \omega t)] \tag{2.3}$$

$$H_\mathrm{d} = (0, H_{y\mathrm{d}}, 0) \exp(-k_{z\mathrm{d}} z) \exp[\mathrm{i}(k_x x - \omega t)], \tag{2.4}$$

when $z < 0$, one has

$$E_\mathrm{m} = (E_{x\mathrm{m}}, 0, E_{z\mathrm{m}}) \exp(k_{z\mathrm{m}} z) \exp[\mathrm{i}(k_x x - \omega t)] \tag{2.5}$$

$$H_\mathrm{m} = (0, H_{y\mathrm{m}}, 0) \exp(k_{z\mathrm{m}} z) \exp[\mathrm{i}(k_x x - \omega t)]. \tag{2.6}$$

Considering equations (2.3) and (2.5) in terms of the Maxwell equation $\nabla \cdot \boldsymbol{E} = 0$, the electric field components take the form

$$E_{z\mathrm{d}} = \mathrm{i}\frac{k_x}{k_{z\mathrm{d}}} E_{x\mathrm{d}} \tag{2.7}$$

$$E_{z\mathrm{m}} = -\mathrm{i}\frac{k_x}{k_{z\mathrm{m}}} E_{x\mathrm{m}}. \tag{2.8}$$

On the other hand, we consider equations (2.3) and (2.4) and apply the Maxwell equation as follows:

$$\nabla \times E = -\frac{1}{c}\frac{\partial H}{\partial \mathrm{t}}. \tag{2.9}$$

Then we have

$$-k_{z\mathrm{d}} E_{x\mathrm{d}} - \mathrm{i}k_x E_{z\mathrm{d}} = \mathrm{i}k H_{y\mathrm{d}} \tag{2.10}$$

where $k = \omega/c$ is the wavevector in free space. Similarly, considering equations (2.5), (2.6) and (2.9), we have

$$k_{z\mathrm{m}} E_{x\mathrm{m}} - \mathrm{i}k_x E_{z\mathrm{m}} = \mathrm{i}k H_{y\mathrm{m}}. \tag{2.11}$$

In terms of equations (2.7) and (2.8), equations (2.10) and (2.11) can be expressed as follows, respectively:

$$\varepsilon_\mathrm{d} k E_{x\mathrm{d}} = \mathrm{i}k_{z\mathrm{d}} H_{y\mathrm{d}} \tag{2.12}$$

$$\varepsilon_\mathrm{m} k E_{x\mathrm{m}} = -\mathrm{i}k_{z\mathrm{m}} H_{y\mathrm{m}} \tag{2.13}$$

where

$$k_{z\mathrm{d}}^2 = k_x^2 - \varepsilon_\mathrm{d} k^2 \tag{2.14}$$

$$k_{z\mathrm{m}}^2 = k_x^2 - \varepsilon_\mathrm{m} k^2. \tag{2.15}$$

Furthermore, we note that the tangential components of $\boldsymbol{E}$ and $\boldsymbol{H}$ are continuous according to the boundary conditions of the electromagnetic fields at $z = 0$, i.e. we have $E_{x\mathrm{d}} = E_{x\mathrm{m}}$, $H_{y\mathrm{d}} = H_{y\mathrm{m}}$; the relationship between the dielectric constants and the normal components of the wavevectors in the two media is given by

$$\frac{k_{z\mathrm{d}}}{k_{z\mathrm{m}}} = -\frac{\varepsilon_\mathrm{d}}{\varepsilon_\mathrm{m}}. \tag{2.16}$$

In terms of equations (2.14), (2.15) and (2.16), we have

$$k_x = k\sqrt{\frac{\varepsilon_\mathrm{d}\varepsilon_\mathrm{m}}{\varepsilon_\mathrm{d} + \varepsilon_\mathrm{m}}}. \tag{2.17}$$

If we substitute k_spp for k_x, the SPP dispersion relation can be expressed as

$$k_\mathrm{spp} = k\sqrt{\frac{\varepsilon_\mathrm{d}\varepsilon_\mathrm{m}}{\varepsilon_\mathrm{d} + \varepsilon_\mathrm{m}}}. \tag{2.18}$$

The SPP dispersion curve exhibits a nonlinear characteristic (figure 3). The momentum ($\hbar k_\mathrm{spp}$) of the SPP wave is larger than that of the light in free space photon ($\hbar k$) for the same frequency, which results in a momentum mismatch between light and SPP. The mismatch must be overcome by coupling light and SPP modes at the interface when

$$\varepsilon_\mathrm{d} + \varepsilon_\mathrm{m} = 0. \tag{2.19}$$

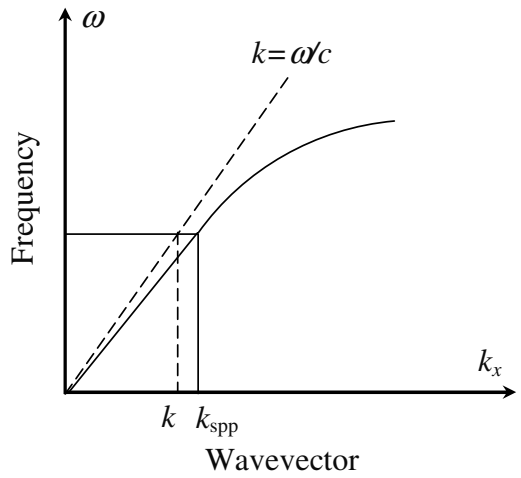

Figure 3. Dispersion curve of a SPP wave, k_{spp} and k are the SPP and free-space wavevectors, respectively, the momentum ($\hbar k_{spp}$) of the SPP wave is larger than that of the light in free space photon ($\hbar k$) for the same frequency (ω).

The surface charges can generate collective oscillation and SPPs can be excited. The dielectric constant of the metal ε_m has the free electron form

$$\varepsilon_m = 1 - \frac{\omega_p^2}{\omega^2} \tag{2.20}$$

where ω_p is the frequency of the bulk plasma. For many metals the frequency is in the ultraviolet wavelength region, while the metal is no longer metallic beyond the frequency. In terms of equations (2.19) and (2.20), the SPP frequency is given by

$$\omega_{spp} = \frac{\omega_p}{\sqrt{1+\varepsilon_d}}. \tag{2.21}$$

It can be seen that the SPP frequency is lower than the bulk plasma frequency.

As mentioned above, the excited SPP waves have associated evanescent fields penetrating into both the dielectric and the metal. They are spatially decaying fields in a direction normal to the interface (figure 2), and the decaying fields of the SPP wave in the dielectric and the metal satisfy equations (2.3) and (2.5), respectively. In this case, the penetration depths in the dielectric and the metal δ_d and δ_m are correspondingly defined by $\delta_d = 1/k_{zd}$ and $\delta_m = 1/k_{zm}$ at which the electric fields fall to $1/e$. In terms of equations (2.14) and (2.17), the penetration depth δ_d of the SPP wave into the dielectric is given by

$$\delta_d = \frac{1}{k}\left|\frac{\varepsilon_d+\varepsilon_m}{-\varepsilon_d^2}\right|^{\frac{1}{2}} \tag{2.22}$$

while, in terms of equations (2.15) and (2.17), the penetration depth δ_m of the SPP wave into the metal is given by

$$\delta_m = \frac{1}{k}\left|\frac{\varepsilon_d+\varepsilon_m}{-\varepsilon_m^2}\right|^{\frac{1}{2}}. \tag{2.23}$$

Furthermore, the penetration depths can be estimated based on equations (2.22) and (2.23). For example, if the metal and the dielectric are silver and silicon oxide, respectively, for 620 nm wavelength ($\varepsilon_d = 2.127$ and $\varepsilon_m = -15.037 + i1.017$ [18]), $\delta_d = 167.0$ nm and $\delta_m = 23.6$ nm, while for 400 nm wavelength ($\varepsilon_d = 2.160$, $\varepsilon_m = -3.773 + i0.675$ [18]), $\delta_d = 39.0$ nm and $\delta_m = 22.0$ nm. We note that the penetration depth in the dielectric is larger than that in the metal, and the difference in the penetration depths becomes quite distinct for long wavelengths (e.g. 620 nm). Considering equations (2.3) and (2.5), $E_d \propto \exp(-k_{zd}z)$ for $z > 0$, and $E_m \propto \exp(k_{zm}z)$ for $z < 0$. It can be seen that the electric fields of SPP wave decay exponentially with distance $|z|$ from the interface. Based on the short penetration depths of the electric fields of SPP wave in the dielectric and the metal, the electric fields of SPP are concentrated mainly near the interface, and the field concentration is remarkably enhanced at the interface. Nevertheless, the field concentration of SPP becomes rapidly low away from the interface along the z direction, and the field concentration is larger in the dielectric than in the metal.

The excitation of SPPs described above occurs at a single interface between the dielectric and the metal. In contrast, a thick metal film bounded by a dielectric can excite two independent SPP waves at two interfaces involving the dielectric and the metal. In this case, the evanescent fields of the two uncoupled SPP waves into the metal cannot overlap [21]. However, when the metal film becomes thin enough, the evanescent fields of the two SPP waves into the metal begin to overlap, and the coupling of the two SPP waves appears between the two interfaces. As a result, the SPP waves split into two supermodes (coupled modes) consisting of one symmetric mode (low-frequency) and one antisymmetric mode (high-frequency) with transverse electric field distributions (figure 4) [22]. Furthermore, for the symmetric SPP mode, the loss of electric fields is very small because the electric fields penetrate more deeply into the dielectric, and the attenuation of the electric fields is much lower (at least a factor of 2–3) than that of the SPP at the single interface. Therefore, the symmetric SPP mode is also called the long-range SPP (LRSPP) [22, 23], and the propagation length of the LRSPP is very long and is 138 times longer than that of the single-interface SPP in the corresponding semi-infinite structure [24], and the length even reaches the order of centimetres [24, 25]. However, for the antisymmetric SPP mode, the loss of electric fields is very large because the electric fields are concentrated mainly into the metal and the SPP modes show increasing confinement. Therefore, the antisymmetric SPP mode is also called the short-range SPP (SRSPP), and the propagation length of the SRSPP is quite short due to the very strong attenuation resulting from the large ohmic losses in the metal. For example, in the Ag–SiO_2 system, for a 20 nm thick metal film and 1550 nm wavelength, the mode power attenuation coefficients of the LRSPP and the SRSPP modes are 0.0012 dB μm^{-1} and 0.45 dB μm^{-1} (2.8 cm^{-1} and 103 cm^{-1}), respectively [26].

2.2. *Coupling to surface plasmon polaritons*

The interaction between the electromagnetic field and the surface charges results in an increase in the SPP momentum compared with that of the free space according to the

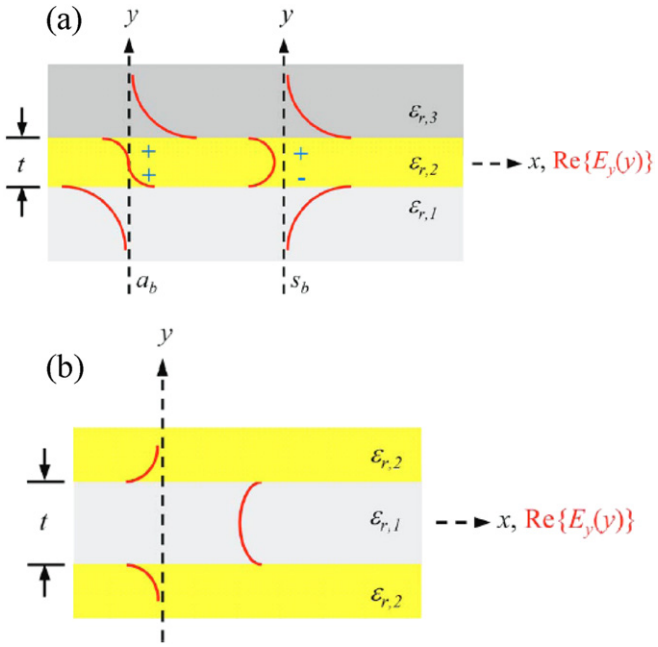

Figure 4. (*a*) Metal slab ($\varepsilon_{r,2}$) of thickness t bounded by semi-infinite dielectrics ($\varepsilon_{r,1}$, $\varepsilon_{r,3}$) supporting two bound SPP modes (a_b, s_b). (*b*) Dielectric slab ($\varepsilon_{r,1}$) of thickness t bounded by semi-infinite metals ($\varepsilon_{r,2}$) supporting a symmetric bound mode. The distribution of the main transverse electric field component of the modes is shown as red curves over the cross-section of each structure.

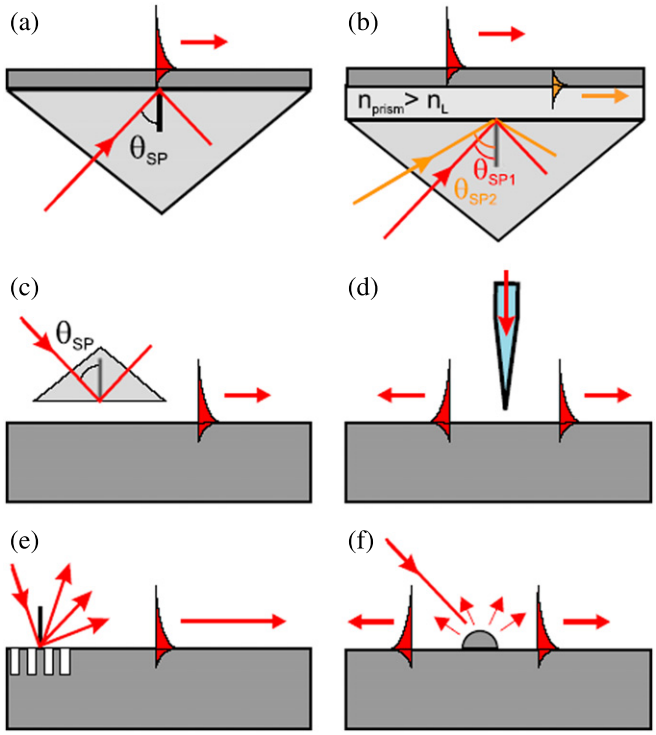

Figure 5. SPP excitation configurations: (*a*) Kretschmann geometry, (*b*) two-layer Kretschmann geometry, (*c*) Otto geometry, (*d*) excitation with an SNOM probe, (*e*) diffraction on a grating and (*f*) diffraction on surface features.

SPP dispersion relation (equation (2.18)), which gives rise to the momentum mismatch between light and SPP. The momentum of light and SPP can be matched using different coupler configurations such as prism couplers [20, 23], grating couplers [20, 23], fibre and waveguide couplers [27–30].

The metal film is illuminated through the dielectric prism at an angle of incidence greater than the critical angle or the total internal reflection angle in the Kretschmann configuration (figure 5(*a*)) [9]. The light wavevector increases in the optically dense medium at a certain incident angle larger than the critical angle. The in-plane component of the light wavevector in the prism coincides with the SPP wavevector on an air–metal surface, which gives rise to the light tunnelling through the metal film, and as a result, the light is coupled to the SPP. Furthermore, the efficiency of SPP excitation decreases with increasing film thickness due to the increase in the tunnelling distance. Figure 5(*b*) shows a two-layer geometry (a dielectric layer with a refractive index smaller than that of the prism is deposited between the prism and the metal film), and using this geometry, the light tunnelling through this dielectric layer can excite SPPs on the internal metal interface at different incident angles. For a thick metal film, Kretschmann configuration cannot be used to excite SPPs; Otto configuration can overcome the problem by placing the prism close to the metal surface (figure 5(*c*)). In this case, light tunnelling occurs through the air gap between the prism and the surface [8]. On the other hand, the diffraction effects by a diffraction grating can satisfy the momentum matching conditions (figures 5(*e*) and (*f*)). The diffracted orders from the periodically corrugated metal–dielectric interface exhibit larger wave vectors in magnitude than those of the incident light, and as a result, the diffraction of light by the metal grating will be coupled to the SPP [1].

Considering the principle of SPP excitation based on total internal reflection with a prism coupler, the coupling prism can be replaced by a waveguide layer of a fibre core; therefore, the light can be coupled to the SPP using a fibre coupler. The cladding of the fibre is removed and it is coated with a metal layer, which is surrounded by a dielectric sensed medium [28–30]. This coupling of the evanescent field with SPP strongly depends upon the light wavelength, fibre parameters, fibre geometry and metal layer properties [30]. For example, the coupling mechanism will be different for single-mode and multi-mode optical fibres due to different mode transmission properties. In particular, a straight fibre and a tapered fibre exhibit different strengths of light coupling because these fibres show different penetration depths of the evanescent field due to different geometrical configurations. The advantages of optical fibre couplers are mainly that they are miniaturized and flexible.

In addition, the light can also be coupled to the SPP using an optical waveguide coupler. The process of exciting SPPs using a optical waveguide is similar to that in the Kretschmann configuration (figure 5(*b*)) [27, 28]. The light is guided by either a single or multilayer (slab or channel) waveguide into a region with a thin metal overlayer, and the light penetrates evanescently through the metal layer. If the SPP and the guided mode can be phase-matched, the incident light excites the SPP at the outer interface of the metal layer.

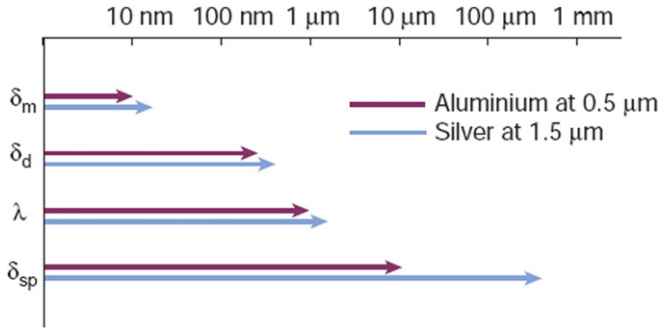

Figure 6. Comparison of the propagation lengths of SPPs between silver and aluminium.

2.3. Propagation of surface plasmon polaritons

Once light has been converted into an SPP mode on a flat metal surface it will propagate, but will gradually attenuate owing to losses arising from absorption in the metal. The propagation length of the SPP is thereby limited by the imaginary part of the complex SPP wavevector k_{spp} due to the internal damping (ohmic losses), where $k_{spp} = k_{sppr} + ik_{sppi}$. Based on the SPP dispersion relation (equation (2.18)), the propagation length of SPP δ_{spp} is given by [12, 31]

$$\delta_{spp} = \frac{1}{2k_{spp\,i}} = \frac{\lambda}{2\pi}\left(\frac{\varepsilon_{mr}+\varepsilon_d}{\varepsilon_{mr}\varepsilon_d}\right)^{3/2}\frac{\varepsilon_{mr}^2}{\varepsilon_{mi}} \qquad (2.24)$$

where ε_{mr} and ε_{mi} are the real and imaginary parts of the dielectric function of the metal, respectively, that is, $\varepsilon_m = \varepsilon_{mr} + i\varepsilon_{mi}$. where δ_{spp} is the distance after which the SPP intensity decreases to $1/e$ of its starting value. The propagation length is usually dependent on the dielectric constant of the metal and the incident wavelength based on equation (2.24). For example, for a relatively absorbing metal such as aluminium the propagation length is 2 μm at a wavelength of 500 nm, while for a low loss metal such as silver, at the same wavelength it is up to 20 μm (figure 6). In addition, for a longer incident wavelength, such as the near-infrared telecom wavelength 1.55 μm, the propagation length of silver increases towards 1 mm.

3. Applications of surface plasmon polaritons

Controlling light on scales much smaller than the light wavelength can be achieved by excitation of SPPs, owing to their unique optical properties described above. SPPs exhibit potential applications in subwavelength optics (e.g. waveguides [32–40] and sources [41–45]), near-field optics [46–63], SERS [64–72], data storage [15, 73–75], solar cells [76–79], chemical sensors [27, 80–84] and biosensors [85–98].

3.1. SPP waveguides

Quinten, Aussenegg and co-workers proposed a subwavelength optical waveguide by a linear chain of spherical silver nanoparticles [32]. Light transport of the long linear chain with constant spacing of spheres was calculated by the Mie theory. When the first particle in the chain is irradiated by

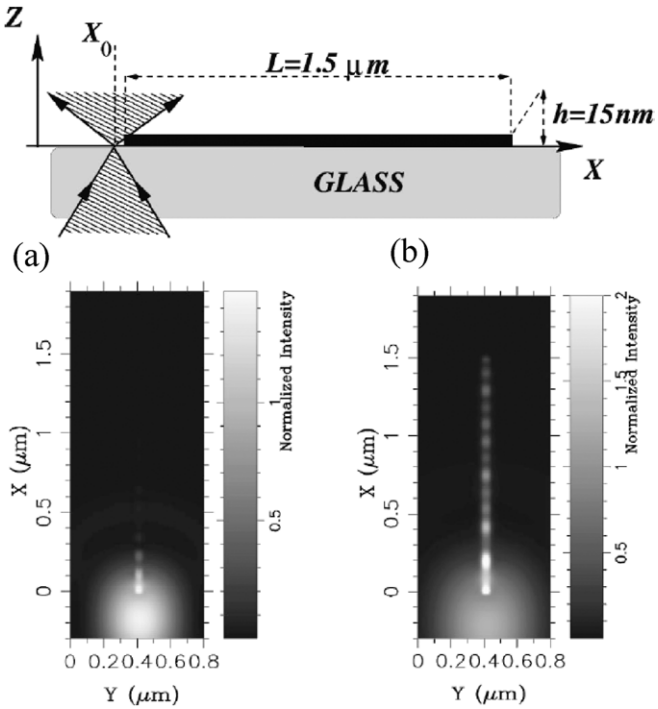

Figure 7. Side view of the illumination condition and electric near-field map computed 10 nm over the top of the nanowire, (*a*) out of resonance, $\lambda = 633$ nm, (*b*) at resonance, $\lambda = 835$ nm.

light field polarized parallel and perpendicular to the chain axis, the efficient guiding light can be observed for the irradiation polarized parallel to the chain axis, and the intensity distribution along the line constantly decreases, whereas the guiding light is strongly damped for the irradiation perpendicular to the chain axis. This is because other spheres get their SPP oscillation energy by coupling for the irradiation at parallel polarization; however, the other spheres cannot guide light without coupling of SPP for the irradiation at perpendicular polarization.

On the other hand, metal nanowires deposited on a transparent substrate can also propagate light [34]. Figure 7 shows the spatial distribution of the near-field intensity over the nanowire for two incident wavelengths of 633 and 835 nm. The observation plane is located 10 nm over the top of the nanowire. For the incident wavelength of 633 nm, the electric field intensity along the x direction is strongly damped. Only the area of the nanowire directly illuminated by the incident spot appears in the near-field map. For a distance of 250 nm from the 'entrance' of the nanowire, the detected intensity is reduced to 10% of the normalized intensity. However, for the incident wavelength of 835 nm, a kind of standing-wave pattern over the nanowire can be observed. The normalized intensity exhibits a strongly oscillating behaviour, and the normalized intensity 1.4 mm away from the 'entrance' end of the nanowire is still 40%. Therefore, the nanowire can be regarded as a subwavelength waveguide for the excitation with a longer wavelength.

Recently, Oulton, Zhang and co-workers have proposed a new approach that integrates dielectric waveguide with SPPs [36]. The hybrid optical waveguide consists of dielectric

nanowires separated from a metal surface by nanoscale dielectric gap. The coupling between the SPP mode and the waveguide mode across the gap enables 'capacitor-like' energy storage and allows effective subwavelength transmission in non-metallic regions. In this case, SPP can travel over large distances (40–150 μm) with strong mode confinement and low propagation loss (ranging from $\lambda^2/400$ to $\lambda^2/40$). Furthermore, the propagation length can increase up to the millimetre range while still maintaining moderate confinement by tuning the geometrical properties of the structure. Pyayt *et al* presented an integration of multiple silver nanowire SPP waveguides with polymer optical waveguides for nanoscale confinement and guiding of light on a chip [37]. They arranged the nanowires perpendicular to the polymer waveguide with one end inside the polymer. Their calculations and experiments indicated that the polarization of incident light affected the degree to which it coupled into the nanowire as a propagating SPP mode. The major advantage of this device is that the same polymer waveguide can be used to couple light into many nanowires in parallel, simultaneously providing light to a number of nanoscale photonic devices in highly integrated photonic circuits.

In addition to the nanoparticles and nanowires for design of SPP waveguides, nanochannels with multiplicate shapes can also be used in propagation SPP. For instance, Bozhevolnyi, Ebbesen and co-workers designed various subwavelength waveguide structures [38, 39], which include V-grooves with angles close to 25° and depths of 1.1–1.3 μm fabricated by focused ion-beam milling in a 1.8 μm thick gold layer deposited on a substrate of fused silica, Y-splitters composed of two mirrored curved bends connecting two parallel waveguides offset with respect to each other (so-called S-bends) and Mach–Zehnder interferometers composed of two consecutive Y-splitters (figure 8). The V-groove SPP structure demonstrates low-loss (propagation length of 100 μm) and well-confined (mode width of 1.1 μm) channel SPP guiding along a triangular 0.6 μm-wide and 1 μm-deep groove in gold (figure 9), and a strong confinement and a sufficiently low propagation loss are achieved simultaneously. Moreover, the channel SPP-based Y-splitters, Mach–Zehnder interferometers and waveguide-ring resonators are operated at telecom wavelength and perform well over the whole range of laser tenability. Furthermore, these channel SPP structures exhibit single mode and subwavelength guiding with overall losses of a few dB at telecom wavelengths. The channel SPP guides can indeed be used for large-angle bending and splitting of radiation.

Since SPP propagation loss is dependent on the surface roughness of noble metal nanostructures, fabrication of smooth surface and high-quality patterned metals is indispensable. Recently, Nagpal, Norris and co-workers have combined template stripping with precisely patterned silicon substrates to obtain ultrasmooth pure metal films with grooves, bumps, pyramids, ridges and holes [40]. The measured SPP propagation lengths on the resulting surfaces approach theoretical values for perfectly flat films, and the structures exhibit Raman scattering enhancements above 10^7 for sensing applications and multilayer films for optical metamaterials.

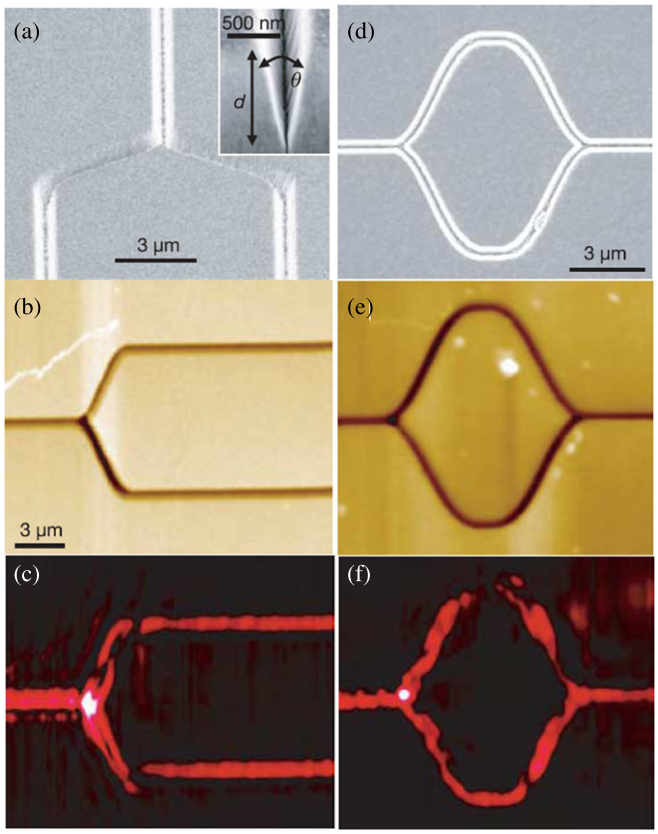

Figure 8. Plasmonic Y-splitter and Mach–Zehnder (MZ) interferometer. (*a*) SEM image, along with (*b*) topographical and (*c*) near-field optical ($\lambda = 1600$ nm) SNOM images of the Y-splitter, inset in (*a*): SEM image showing the typical groove profile (d and θ are the groove depth and angle, respectively). (*d*)–(*f*) Same as (*a*)–(*c*) but for the MZ interferometer.

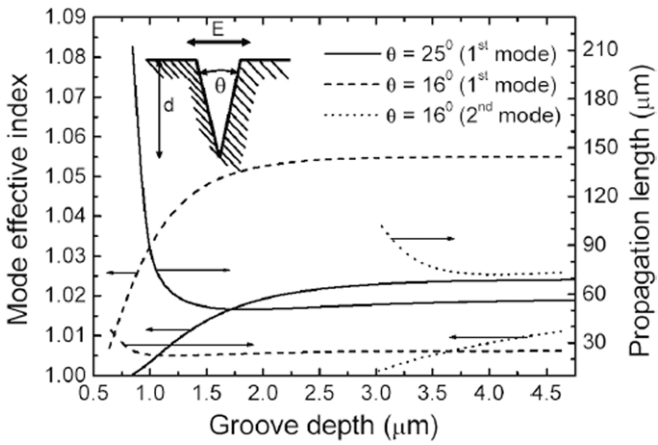

Figure 9. Effective indices of CPP modes and their propagation lengths as a function of groove depth d for different groove angles θ; the inset shows the groove configuration and dominant orientation of the CPP electric field.

3.2. SPP sources

Lezec, Ebbesen and co-workers proposed a periodic bull's eye structure on the exit side of a single hole in a metal film to obtain a beam with a small angular divergence by the focused ion-beam (FIB) milling technique [41]. The cylindrical hole with

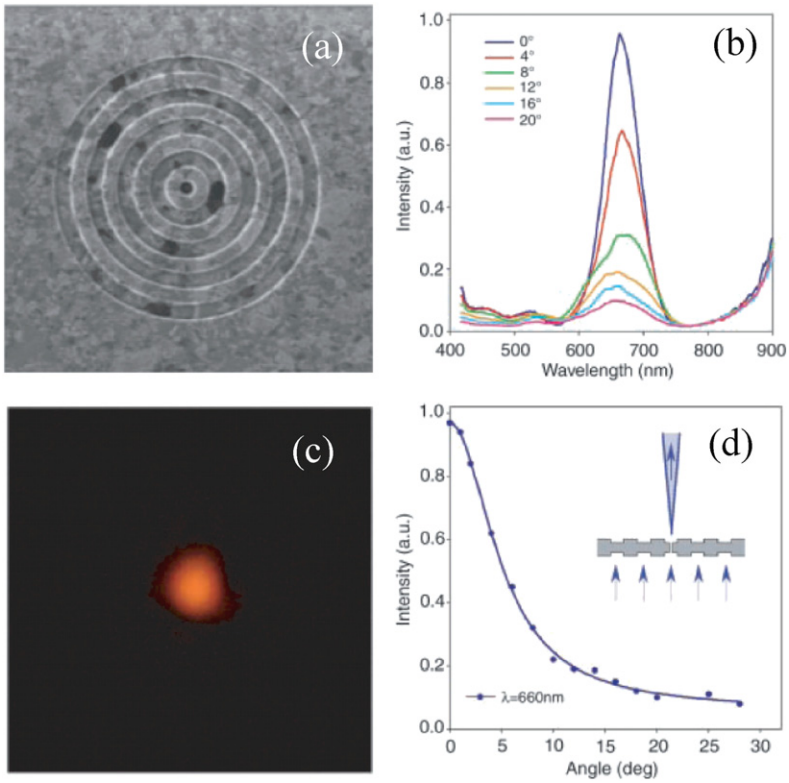

Figure 10. (*a*) FIB micrograph image of a bull's eye structure surrounding a cylindrical hole in a suspended Ag film (groove periodicity, 500 nm; groove depth, 60 nm; hole diameter, 250 nm; film thickness, 300 nm). (*b*) Transmission spectra recorded at various collection angles for the bull's eye structure on both sides of the Ag film. (*c*) Optical image of the sample illuminated from the back at its wavelength of peak transmission ($\lambda_{max} = 660$ nm) using a 50 nm band-pass filter. (*d*) Angular transmission intensity distribution derived from the spectra of (*b*) at λ_{max}. (Inset) schematic diagram of the structure and the beam divergence and directionality of the transmitted light at λ_{max} in the far field.

a diameter of 250 nm in a suspended silver film was surrounded by a periodical groove with a periodicity of 500 nm and depth of 60 nm. The free-standing suspended film with a thickness of 300 nm was used to allow patterning of both input and exit sides independently (figure 10(*a*)). For a single cylindrical hole, the transmission measurement demonstrates that the exiting light is fully diffracted into a half-sphere. When the input side around the hole is patterned with a concentric periodic groove structure (bull's eye), the transmission is boosted at wavelengths determined by the periodic corrugation due to coupling to SPP, but the light remains fully diffracted as in the case of the bare hole. Nevertheless, a strong transmission peak around 660 nm was observed for illumination at normal incidence when an identical bull's eye grating of the same period was patterned around the exit side of the hole due to coupling to SPP (figure 10(*b*)), and a strong dependence of angle was observed by recording the transmission spectra at various angles on the exit side. Moreover, a plot of the transmission intensity as a function of angle (figure 10(*d*)) implies that the transmitted light emerges in the shape of a well-defined beam with a beam divergence of $\pm 3^{\circ}$. Therefore, the periodic bull's eye structure of the silver film can be worked as a SPP source due to a combination of low divergence, directionality and high efficiency.

There is an increasing requirement for miniaturization of laser elements. Recent advances are microscopic lasers that can reach the diffraction limit based on photonic crystals [99], metal-clad cavities [100] and nanowires [101, 102]. However, these lasers in optical mode size and device dimension are larger than the half-wavelength of the light. It remains a fundamental challenge to realize ultracompact lasers that can directly generate coherent optical fields beyond the diffraction limit. Recently, Oulton, Zhang and co-workers have presented a SPP laser at the deep subwavelength scale [44]. The lasers were designed using a hybrid SPP waveguide consisting of a high-gain CdS semiconductor nanowire on top of a silver substrate, separated from a silver surface by a nanometre-scale MgF_2 insulating layer with a thickness of 5 nm (figure 11(*a*)). They optically pumped the SPP laser elements at a wavelength of 405 nm and measured emission from the dominant I_2 CdS exciton line at 489 nm (figure 11(*b*)). The onset of amplified spontaneous emission peaks was observed at moderate pump intensities (10–60 MW cm^{-2}), and the emission is the longitudinal cavity modes that form when propagation losses are compensated by gain, allowing SPP modes to resonate between the reflective nanowire end-facets. In this case, the multiple cavity mode resonance at higher pump powers demonstrates sufficient material gain to achieve full laser oscillation. In addition, the emission lifetime measurements reveal a broadband enhancement of the nanowire's exciton spontaneous emission rate by up to six times owing to the strong mode confinement and the signature of apparently threshold-less lasing. This deep subwavelength SPP laser action at visible frequencies suggests new sources that may produce coherent light far below the diffraction limit.

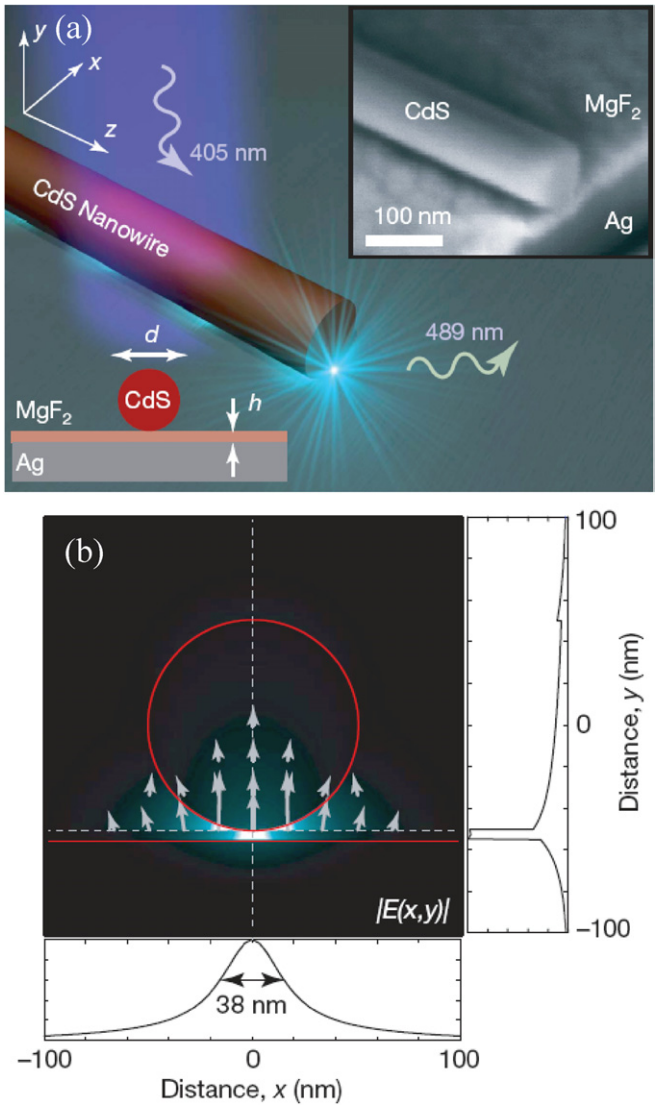

Figure 11. Deep subwavelength plasmonic laser. (*a*) Plasmonic laser consists of a CdS semiconductor nanowire on top of a silver substrate, separated by a nanometre-scale MgF_2 layer. This structure supports a new type of plasmonic mode, and the mode size is a hundred times smaller than a diffraction-limited spot; the inset is an SEM image of the plasmonic laser. (*b*) The stimulated electric field distribution and direction $|E(x, y)|$ of a hybrid plasmonic mode at a wavelength of 489 nm. The cross-sectional field plots illustrate the strong overall confinement in the gap region between the nanowire and metal surface with sufficient modal overlap in the semiconductor to facilitate gain.

3.3. Near-field optics

A scanning near-field optical microscope (SNOM) can control and observe light at nanometre scale resolution, which is much smaller than the half-wavelength of light resolution typically achieved by conventional optical microscopes. It is noted that the key element of SNOM is the probe serving as an emitter, collector or scatterer of light. The usual SNOM probe is a small hole formed on the end of a metal-coated tapered optical fibre; however, the efficiency of the SNOM probe is limited by the small amount of light that can be coupled through the hole, and the signal from very small objects on the sample surface is very weak by the probe. Ketterson and co-workers presented a SNOM based on SPPs [46, 47]. First, an electrochemically etched tungsten filament was used as the probe tip, then a silver film of 50 nm thickness was sputtered onto a microscope cover glass. In this case the SPPs was excited on the film surface in the Kretschmann total internal reflection configuration. As a result, enhanced fields were localized at individual surface irregularities by the scattering of SPPs and the scattered SPPs produce a conical radiation. In this case a small scatterer works as a probe to avoid the problems associated with a hole, and exploits SPPs to enhance the signal and improve the collection efficiency.

If metal structure can be made much smaller than the light wavelength, one can scan such a nanostructure along the sample surface as a probe and image a sample with high-resolution geometry, similar to the other scanning probe microscopes. The SPP of a metal nanoparticle is strongly localized, and the localized SPP modes in a small metal structure can couple with the propagating photons [53], which essentially means slowing down of the light or reduction in the effective wavelength close to the metal nanostructure. Any microscopy involving this confined light field will therefore have a spatial resolution comparable to the size of the confined field, which is the same as the size of the metal nanostructure.

Conventional immersion lenses are limited by materials with high refraction index for enhancement of image resolution. In contrast, optical imaging can be achieved through a thin metal slab [48]; for a 120 nm thick silver slab as a lens placed 60 nm below a patterned mask, optical images with feature sizes as small as 350 nm (at a 700 nm period) can be obtained on a photosensitive material. Moreover, a superlens operating in the near-field region can substantially enhance the electric fields of the evanescent waves for imaging owing to the excitation of SPPs [49, 50]. Zhang and co-workers reported optical imaging below the diffraction limit using a silver superlens [51, 52]. A set of embedded objects were inscribed onto a chrome mask, which was patterned on quartz and then planarized by FIB lithography, and a 40 nm-thick layer of polymethyl methacrylate (PMMA) spacer layer was used between the chrome masks and a 35 nm silver film. Finally, the embedded objects were imaged onto the photoresist on the other side of the silver film under ultraviolet (UV) illumination with a wavelength of 365 nm. In this case, the silver superlens can image arbitrary nanostructures with sub-diffraction-limited resolution. The recorded image 'NANO' shows that the fine features can be reproduced with good fidelity. In addition, a broad spectrum of subwavelength features can be achieved by proper design of the working wavelength and thickness of the silver film. As a result, a sub-diffraction-limited imaging with 60 nm half-pitch resolution (one-sixth of the illumination wavelength) can be performed by the silver superlens.

Optical and infrared antennas based on metal nanostructures allow efficient conversion of propagating light into nanoscale confined and strongly enhanced optical fields [103, 104]. Antennas consisting of adjacent metallic nanorods separated by a gap antenna are particularly efficient [54, 103]. Schnell, Hillenbrand and co-workers proposed a

SPP nanoantenna consisting of gold nanorods designed for fundamental dipolar resonance at mid-infrared frequencies [55]. A strong amplitude signal was achieved at the nanorod extremities and an anti-phase field oscillation was expected for the dipolar near-field mode. The scattering-type SNOM based on SPP nanoantennas provides direct experimental evidence to monitor the evolution of the near-field oscillations. In addition, Yagi–Uda antennas can exhibit high directivity, which are directional antennas consisting of a driven element (a dipole or a feed) and additional parasitic elements (usually a reflector and one or more directors). Recently, Kosako *et al* experimentally demonstrated directional control of radiation by an optical Yagi–Uda nanoantenna composed of an appropriately tuned gold nanorod array [56, 57]. A high directivity can be obtained with distances of about 0.25λ between the feed and the reflector and about 0.3λ between the feed and the director and between the directors [58]. The nanoantenna can guide the emission of light from a nanoemitter using metal nanostructures with a total size that is not much larger than the wavelength. The directionality of emission can be significantly improved by a simple arrangement of the two element antennas. Li, Engheta and co-workers presented an optical spectrum analyser at the nanometre scale by optical Yagi–Uda nanoantennas composed of plasmonic core–shell nanoparticle arrays [59]. Yagi–Uda narrow radiation beams operating at different frequencies were obtained based on the scattering phase of the nanoparticles, and the scattering phase can be tuned by changing the ratio of radius in the concentric core–shell nanostructure [60]. Furthermore, Taminiau *et al* exhibited enhanced excitation and emission of single emitters by an optical Yagi–Uda nanoantenna [61]. This is because the single emitter is coupled to the SPP near-field of the feed element. In this case, the emission of the emitters is determined by the nanoantenna modes both in polarization and angular pattern [62]. Enhanced excitation light can also be applied to the enhancement of Raman signals by selecting the shape and spacing of the nanoantennas [63].

3.4. Surface-enhanced Raman spectroscopy

One of the most spectacular applications of SPPs to date is SERS. SERS was first observed by Fleischman in 1974 [105], and discovered by Jeanmarie and Van Duyne [106] and Albrecht and Creighton [107] in 1977. SERS mechanisms may involve electromagnetic enhancement, chemical enhancement or resonance enhancement [17, 64, 66]. One of the most accepted mechanisms of SERS is the electromagnetic enhancement, and it is attributed to the excitation of SPPs [66, 108].

Here, a quantitative explanation by a simple theoretical calculation is presented [66]. The average magnitude of the field radiated for the metal particle $E_s = gE_0$, where g is the field enhancement averaged over the surface of the metal particle, and E_0 is the magnitude of the incident field. One notes that E_s is the average local near-field at the metal particle surface, and the Raman-scattered light produced by the molecules adsorbed at the surface of the metal particle will have a field strength $E_R \propto \alpha_R E_s = \alpha_R g E_0$, where α_R is the appropriate combination of components of the Raman tensor. The Raman-scattered fields can be further enhanced by the metal particle, that is, the metal particle can scatter light at the Raman-shifted wavelength enhanced by a factor g'. Furthermore, the amplitude of the SERS-scattered field will be given by $E_{SERS} \propto \alpha_R g g' E_0$, and the average SERS intensity will be proportional to the square modulus of E_{SERS}. We have $I_{SERS} \propto |\alpha_R|^2 |gg'|^2 I_0$, where I_{SERS} and I_0 are the intensities of the SERS-scattered and incident fields, respectively. For low-frequency modes when $g \approx g'$, the SERS intensity will be enhanced by a factor proportional to the fourth power of the enhancement of the local incident near-field, $|E_L|^4 = |g|^4$. (For higher frequency modes the SERS intensity is a more complicated function of the SPP properties of the metal particle according to the precise wavelengths at which the incident and Raman-scattered light fall.) It is helpful to define the SERS enhancement Gas the ratio of the Raman-scattered intensity in the presence of the metal particle to its value in the absence of the metal particle $G = |\alpha_R/\alpha_{R0}|^2 |gg'|^2$, where α_{R0} is the Raman polarizability of the isolated molecule. Several points should be considered: first, the major contribution to SERS is scattering by the metal particle rather than the molecule reflected in the SERS spectrum of the light scattered; second, although the SERS intensity (for low-frequency Raman modes) varies as the fourth power of the local field, the effect is a linear optical effect, which depends on the first power of I_0. However, the fourth-power dependence on g is key to the inordinate enhancement SERS provides. For example, for silver at 400 nm, g is only 30, yet that implies a Raman enhancement G of 8×10^5 assuming the Raman polarizability to be unchanged from that of the isolated molecule; third, the Raman polarizability of the scatterer that includes not only the molecule adsorbed on the surface of the metal particles but also contributions from the metal particles. As a result, the magnitude, symmetry and resonant properties from the Raman polarizability of the isolated molecule will be significantly altered. This will be particularly important in systems where metal-to-molecule or molecule-to-metal charge transfer occurs, dramatically altering the resonances of the system thereby contributing to so-called chemical enhancements. Finally, it is important to note that the key parameter that controls the enhancement factor for nanoparticles is the size of the gap between the particles. It was found that the Raman enhancement G varies rapidly with gap size of the nanoparticles, and it is only for gaps on the order of 1–2 nm that one can obtain exceptionally large values such as $G = 10^{11}$.

Raman scattering events of single molecules have been recorded using chemically roughened silver surfaces [17, 64]. For single Rhodamine 6G molecules (2×10^{-10}M) adsorbed on individual silver colloidal nanoparticles, the intrinsic Raman enhancement factors are on the order of 10^{14}–10^{15} [17]. The majority of this enhancement is stemmed from the highly enhanced fields in metal nanoparticle junctions due to SPPs. These particles emitted bright, Stokes-shifted (towards longer wavelengths) light and are called hot spots. Strong evidence has been obtained from Raman polarization measurements at the single-particle level. The two selected particles exhibit intense Raman signals with either s- or p-polarized light

(parallel or perpendicular to the plane of incidence) [17], depending on how a particular particle is oriented relative to the polarization axis. These two nanoparticles should have orthogonal orientations due to SPP effects; when one is maximally excited in the direction of s-polarization, the other is minimally excited, and vice versa. The overall excitation polarization contains two contributions: one from the preferential excitation of an oriented nanoparticle, and the other from the preferential excitation of the Raman polarizability tensors of an oriented molecule.

For exploring the SERS enhancement factor of noble metal nanostructures, Fang, Dlott and co-workers measured the distribution of site enhancements for benzenethiolate molecules on a 330 nm silver-coated nanosphere lattice using incident light of 532 nm wavelength [68]. A series of laser pulses with increasing electric fields burned away molecules at sites with progressively decreasing electromagnetic enhancement factors. It was found that the SERS enhancement factor exhibited a broad distribution of local enhancement factors η and satisfied a power law proportional to $\eta^{-1.75}$, with the minimum and maximum values of 2.8×10^4 and 4.1×10^{10}, respectively, and the hottest sites ($\eta > 10^9$) accounted for just 63 in 10^6 of the total but contributed 24% to the overall SERS intensity [68].

Recently, Xu, Zhang and co-workers have demonstrated an ultrasensitive detection of organic molecules based upon SERS effects using periodical silver nanowire arrays embedded in porous anode alumina membranes [69]. We measured Raman signals of Rhodamine 6G molecules with different concentrations (10^{-6}, 10^{-9}, 10^{-12} and 10^{-13}M) adsorbed on the substrate of silver nanowire arrays. It was found that the Raman signals of the Rhodamine 6G molecules with a concentration of 10^{-13}M could still be detected with a visible light (514.5 nm) excitation under a relatively short integration time of 10 s (figure 12) . Furthermore, the SERS signals can be improved by adjusting the parameters (e.g. diameter, spacing and aspect ratio) of the nanowires. In contrast to our substrate, the detection limit of Rhodamine 6G molecules using the traditional substrate of oxidation-reduction cycle (ORC) roughened silver electrodes is only 10^{-9}M [70] (figure 13). Therefore, the as-fabricated SERS substrates are easy to fabricate, low in cost, flexible to adjust and convenient in measurement. The silver nanowire array substrates will exhibit great potential in trace detections of persistent organic pollutants.

In a conventional SERS experiment, the incident laser light is focused onto the SERS hot spots on the metal nanostructure and the emitted Raman light is detected from the same spot. Nevertheless, such an approach would not be feasible in many applications, especially in living systems, where the higher power incident laser light might cause cell destruction or induce a chemical modification of the analyte. Recently, Fang, Xu and co-workers have demonstrated that a junction between a silver nanowire and an adjacent silver nanoparticle can achieve large SERS enhancements [71], and the large SERS signal can be detected from a location that is remote from the illumination point, which is based on propagating SPPs at one end of a silver nanowire as a remote excitation source rather than direct optical excitation.

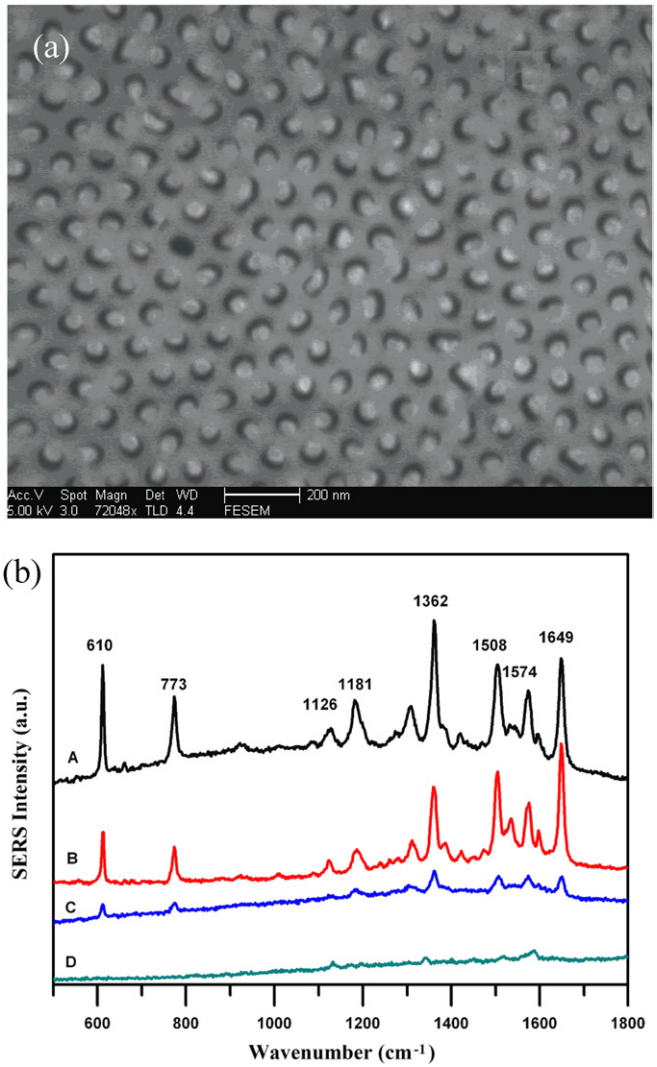

Figure 12. (*a*) SEM images of the silver nanowire arrays embedded in anode alumina membranes used for SERS substrates. (*b*) SERS spectra of the silver nanowire arrays adsorbed R6G molecules with an integration time of 10 s for all samples; A, B, C and D represent molecule concentrations of 10^{-6}M, 10^{-9}M, 10^{-12}M and 10^{-13}M, respectively.

3.5. Data storage

Multiplexed optical recording provides an unparalleled approach to increasing the information density beyond 1 Tbit cm^{-3} by storing multiple, individually addressable patterns within the same recording volume. Wavelength [109, 110], polarization [111, 112] and spatial dimensions [113, 114] have been presented; however, integration of multiplexing is still a significant challenge due to the lack of a suitable recording medium that is extremely selective in the domains of wavelength and polarization and in the three spatial domains. Recently, Zijlstra, Chon and Gu have shown true five-dimensional optical recording by exploiting the unique properties of the longitudinal localized surface plasmon resonance (LSPR) of gold nanorods [15]. It is noted that one of the origins of selecting the noble metal nanorods is their polarization anisotropy, the polarization anisotropy of one-dimensional noble metal nanostructures dependent on

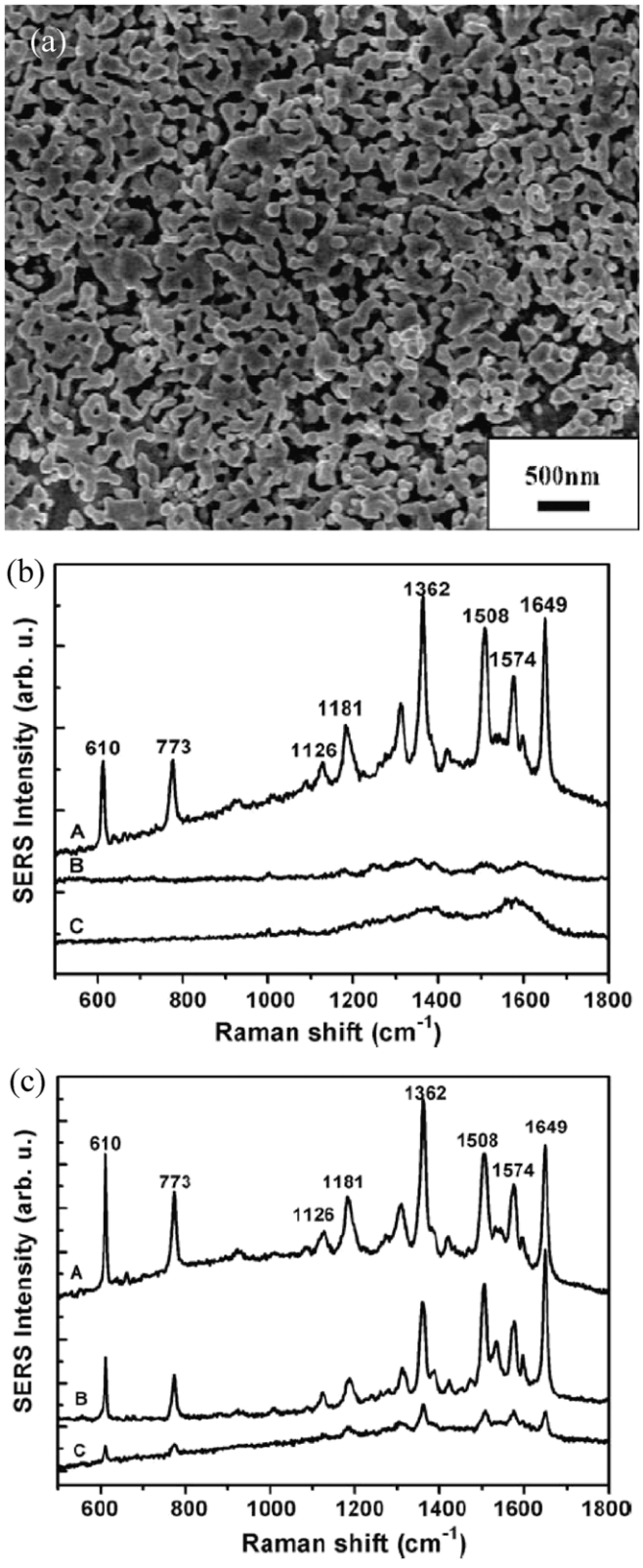

Figure 13. (*a*) SEM image of ORC voltage roughened silver electrode, SERS spectra of ORC voltage roughened silver electrode (*b*) and the silver nanowire arrays (*c*); curves A, B and C in (*b*) and (*c*) correspond to R6G molecule concentrations of 10^{-6}M, 10^{-9}M and 10^{-12}M, respectively.

their sizes has been confirmed at visible and near-infrared wavelengths by our previous study [115, 116]. Furthermore, the concept of five-dimensional patterning is illustrated in figure 14. The sample consists of a multilayered stack in which thin recording layers of 1 μm are separated by a transparent spacer of 10 μm, in both the wavelength and polarization domains. Three-state multiplexing is illustrated to provide a total of nine multiplexed states in one recording layer. One notes that the key to successfully realizing such five-dimensional encoding is a recording material that (1) is orthogonal in all dimensions, in both recording and readout, (2) is able to provide multiple recording channels in each dimension, and (3) is stable under ambient conditions and can be read out non-destructively. They proposed that a recording material based on SPP gold nanorods could satisfy all the above criteria. Longitudinal LSPR exhibits an excellent wavelength and polarization sensitivity and a narrow linewidth (figure 15), and the resonance of the dipolar mode can be achieved by optically addressing only a small subpopulation of nanorods in the laser irradiated region. Moreover, longitudinal LSPR-mediated recording and readout can be governed by photothermal reshaping and two-photon luminescence detection (figure 16), respectively. The recordings using longitudinal LSPR-mediated two-photon luminescence can provide an enhanced wavelength and angular selectivity compared with conventional linear detection mechanisms. Combined with the high cross-section of two-photon luminescence, this enables non-destructive, crosstalk-free readout. The presented technique can be highly beneficial for high-density optical data storage, by decreasing the spacer layer thickness to 1 μm. A disk capacity of 7.2 Tbyte can be obtained and the recording speed is expected up to 1 Gbits^{-1} when a high repetition rate laser source is used.

3.6. Solar cells

Solar cells are also called photovoltaic cells or photoelectric cells. They are solid-state electrical devices that converts the energy of light directly into electricity by the photovoltaic effect. Generally, the photovoltaic absorbers must be optically thick to enable nearly complete light absorption and photocarrier current collection, and these absorbers are usually semiconductors with thicknesses several times the optical absorption length. Furthermore, decreasing the absorber thickness can increase the conversion efficiency, and thin absorber layers are suitable for photovoltaic devices by enabling efficient photocarrier collection across short distances. Thus, this allows the use of low-dimensional structures such as quantum dots and wells. However, for conventional cell designs, efficiencies of nanometre thickness cells are strongly limited by decreased absorption, carrier excitation and photocurrent generation. Therefore, new strategies for enhanced absorption and light trapping are desirable.

Conventional light trapping schemes use wavelength scale surface texturing on the front or back of the cell to enhance light absorption. These structures are too large to be used with extremely thin films. Metal nanostructured thin films

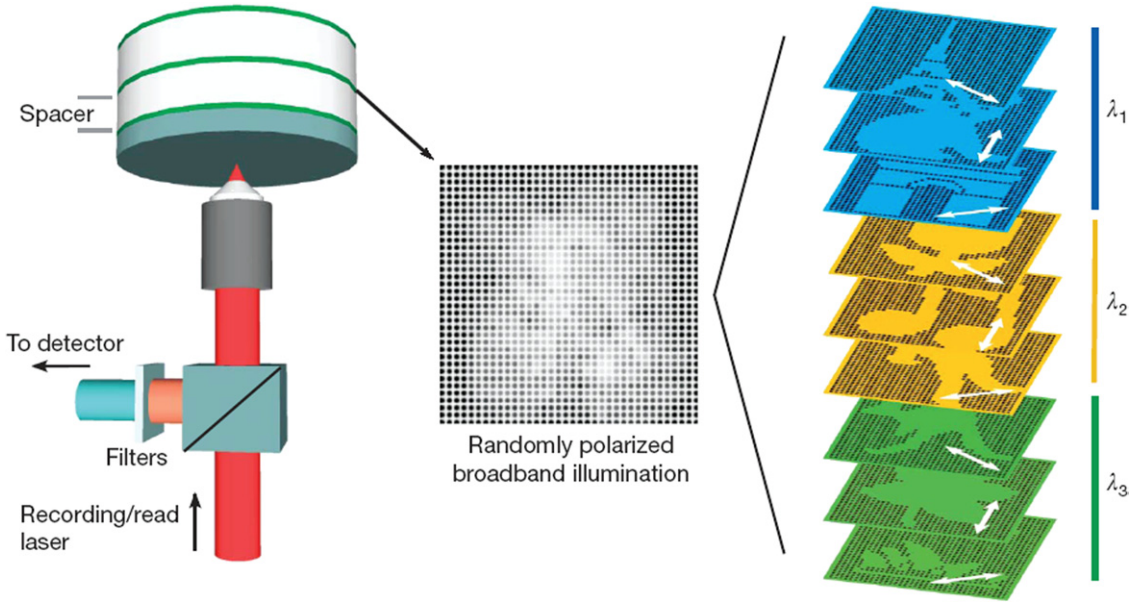

Figure 14. Sample structure and patterning. Left: the sample consists of thin recording layers of spin-coated polyvinyl alcohol doped with gold nanorods; these recording layers were spaced by a transparent pressure-sensitive adhesive with a thickness of 10 μm. In the recording layers, multiple images were patterned using different wavelengths (λ_{1-3}) and polarizations of the recording laser. Middle: when illuminated with unpolarized broadband illumination; a convolution of all patterns will be observed on the detector. Right: when the right polarization and wavelength are chosen; the patterns can be read out individually without crosstalk.

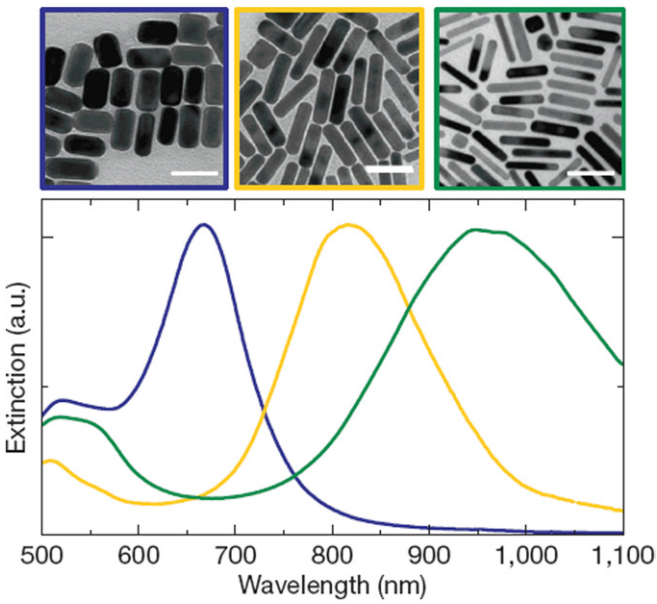

Figure 15. Normalized extinction spectra of the as-prepared gold nanorod solutions. Insets show transmission electron micrographs of the gold nanorods on a copper grid. The average sizes of the nanorods are, from left to right, 37 × 19 nm (aspect ratio 2 ± 1), 50 × 12 nm (aspect ratio 4.2 ± 1) and 50 × 8 nm (aspect ratio 6 ± 2). Scale bars, 50 nm. Each recording layer in the multilayered sample is doped with a mixture of these gold nanorods to form an inhomogeneously broadened extinction profile.

have the potential to confine and guide incident sunlight into subwavelength thickness absorber layer volumes due to excitation of SPPs, and the photovoltaic conversion efficiency of solar cells can be enhanced by incorporation of small metal nanostructures. For instance, the incorporation of metal nanoclusters (silver, gold and copper) at the ITO–CuPc interface can lead to a significant enhancement of the conversion efficiency. For a CuPc layer thickness of about 70 nm, the integral photocurrent enhancement by solar light irradiation is 1.3 for silver clusters, 2.2 for gold clusters and 2.7 for copper clusters [76]. The enhancement of conversion efficiency results from resonant light absorption in the metal clusters. Excitation of SPPs leads to an increased number of photoexcited electrons in the metal which are capable of surmounting the Schottky barrier and therefore increases the short-circuit photocurrent. Westphalen, Meissner and co-workers investigated the influence of excited SPPs in small silver clusters, where the clusters were placed directly in a photovoltaic active Schottky contact formed at the interface of ITO and zinc phthalocyanine (ZnPc) [77]. It was found that the extinction of the ITO/silver clusters/ZnPc system was the superposition of the clusters and the ZnPc bulk absorption. Furthermore, this enhancement with increased absorption of photons in the organic dye layer resulted from the high electric field strength in the vicinity of the excited SPPs, and the incorporated metal clusters led to an increase in the short-circuit current in a spectral region where the cluster film absorbs but the ZnPc does not. Ferry, Atwater and co-workers proposed that subwavelength scatterers could couple sunlight into guided modes in thin film Si and GaAs plasmonic solar cells whose back interface was coated with a corrugated silver thin film [78]. They found that incoupling of sunlight was remarkably insensitive to the incident angle based on a numerical simulation by the finite-difference time domain (FDTD) method, and that the spectral features of coupling efficiency originated from several different resonant phenomena. Moreover, the incoupling cross-section can be spectrally tuned and enhanced through modification of the

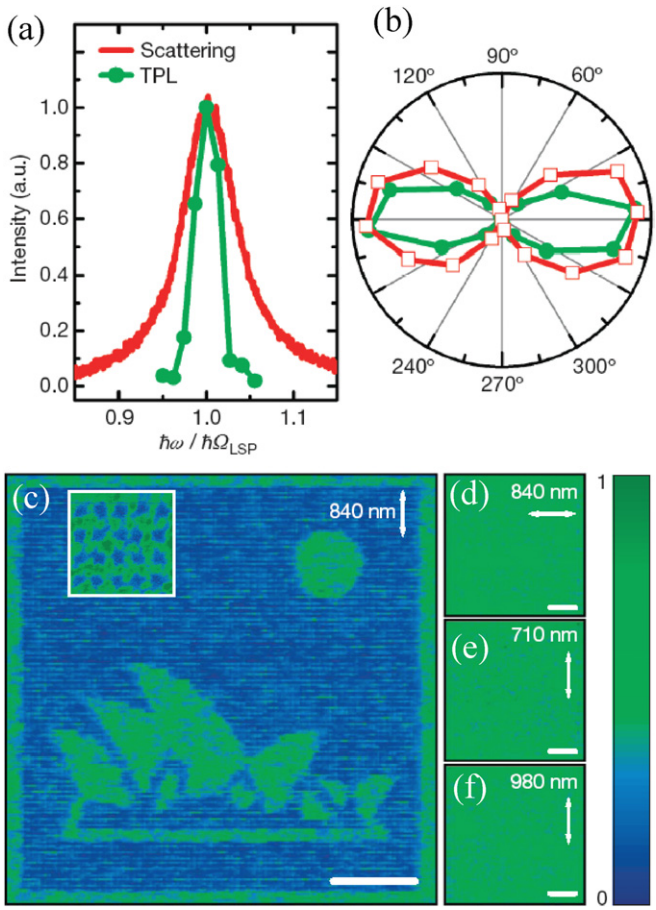

Figure 16. Readout using two-photon luminescence. (*a*) Normalized white light scattering spectrum (red solid line) and two-photon luminescence (TPL) excitation profile (green circles) as a function of photon energy for individual gold nanorods with approximate dimensions of 90×30 nm; the profiles were centred around the longitudinal SPR energy. (*b*) Polarized scattering (open squares) and TPL intensity (filled circles) versus the polarization of the excitation light. (*c*) Normalized TPL raster scan of an image patterned using single laser pulses per pixel with a wavelength of 840 nm and vertical polarization, the TPL was excited with the same wavelength and polarization as was used for the patterning, and the pattern is 75 × 75 pixels, with a pixel spacing of 1.33 μm. Inset: high magnification image of the recording (size 7 × 7 μm). (*d*)–(*f*) Images obtained when the TPL is excited at 840 nm with horizontal polarization (*d*), at 710 nm with vertical polarization (*e*) and at 980 nm with vertical polarization (*f*); scale bars are 20 μm.

scatterer shape, semiconductor film thickness and materials choice. It was demonstrated that 300 nm of Ag with a single 100 nm wide by 50 nm deep groove under a 200 nm thick Si film could enhance absorption by a factor of 2.5 over a 10 μm area for the portion of the solar spectrum near the Si band gap. These findings are promising for the design of ultrathin solar cells that exhibit enhanced absorption.

Very recently, Brown, Snaith and co-workers have demonstrated a method for enabling SPP-enhanced charge generation in dye-sensitized solar cells that are entirely compatible with the state-of-the-art processing and technology and compatible with other photovoltaic concepts [79]. They incorporated core–shell Au–SiO_2 nanoparticles into dye-sensitized solar cells employing both the iodide/triiodide redox couple and the solid-state hole transporter 2,2′,7,7′-tetrakis-(*N*,*N*-di-*p*-methoxyphenylamine)-9,9′-spirobifluorene (spiro-OMeTAD) [117]. Furthermore, the Au–SiO_2 nanoparticles result in an enhanced light absorption and photocurrent generation in dye-sensitized solar cells. They identified that the SPP-enhanced photogeneration of charge carriers could only occur when the electron transfer from the photoexcited dye to the TiO_2 is faster than around 10 fs. It is noted that speeding up electron transfer from the dye and inhibiting possible collisions, which may change the plasmon wave vector in the metal nanoparticles, are key issues to further efficiency enhancement.

3.7. Chemical sensors and biosensors

A chemical sensor is a device that transforms chemical information into an analytically useful signal. The chemical information involves the concentration of a specific sample component to total composition analysis. Due to the increasing number of biological and environmental issues, reliable, sensitive, selective and user-friendly chemical sensors have become more and more attractive [118]. A chemical sensor consists of a transducer whose typical response is significantly altered by the presence of the chemical to be detected. Among various optical methods, SPPs have been widely used. An SPR sensor consists of an optical system, a transducing medium and chemical domains, and also, an electronic system supporting the optoelectronic components of the sensor for data processing; the transducing medium transforms changes in the refractive index determined by optically interrogating the SPP [27].

Since the dielectric constant of the environmental medium has an influence on the SPPs, employing SPPs for chemical detection will rely on the alteration of the surrounding medium. For instance, when a metallic film or nanoparticle is functionalized with a molecular receptor, the environment close to the surface undergoes substantial modifications on trapping the analyte, which triggers detection [27, 80]. Apart from the refractive index of the environment, the capability of a coordinated ligand to increase or decrease the electron density in nanoparticles is a second factor that strongly influences the position of the SPPs [81]. This property was chosen as a transducer for designing new hybrid sensors. Le Floch and co-workers reported synthesis of gold nanoparticles stabilized by sp^2-phosphorus-hybridized ligands, namely a phosphinine [82]. The SPP peak measured for these nanoparticles is strongly red-shifted compared with usual phosphane or thiol-based ligands, and this shift is in good agreement with the strong π-accepting properties of the phosphinine ligand [83]. Therefore, these particles were thought to be ideal candidates for monitoring ligand-exchange processes with phosphanes and thiols. Moreover, they explored these displacement reactions and the sensitivity of the SPP peak for the detection of this exchange [84]. The nanoparticles were immobilized in periodically organized mesoporous silica thin films. Measurement of UV/Vis spectroscopy indicated that exchange with thiol and phosphane resulted in a blueshift of the SPP peak, with a concomitant relative decrease in peak intensity. Therefore, the Au nanoparticles can act as very sensitive and responsive sensors for various chemicals.

The last two decades have witnessed remarkable progress in the development of biosensors and their applications in environmental protection, biotechnology, medical diagnostics, drug screening, food safety and security. A biosensor is an analytical device for the detection of an analyte that combines a biological component with a physicochemical detector component. The biosensor consists of a transducer and a biological recognition element which is able to interact with a selected analyte. Various optical methods have been exploited in biosensors including fluorescence spectroscopy, interferometry, spectroscopy of guided modes of optical waveguides and SPPs [85]. SPP biosensors exhibit various advantages: (1) versatility: SPP sensors can be tailored for detection of any analyte, can provide a biomolecular recognition element, and analyte does not have to exhibit any special properties such as fluorescence or characteristic absorption and scattering bands; (2) no labels required: binding between the biomolecular recognition element and analyte can be observed directly without the use of radioactive or fluorescent labels; (3) speed of analysis: the binding event can be observed in real-time providing potentially rapid response; (4) flexibility: SPP sensors can perform continuous monitoring as well as one-time analyses.

SPP biosensors are optical sensors exploiting SPPs to probe interactions between an analyte in solution and a biomolecular recognition element immobilized on the SPR sensor surface. The propagation length of the SPP is extremely sensitive to changes in the refractive index of the dielectric, and the biomolecular recognition element on the surface of metal recognizes and captures analyte in a liquid sample producing a local increase in the refractive index at the metal surface. Since the refractive index increase gives rise to an increase in the propagation length of the SPP along the metal surface, the detection of the interactions between the analyte and the biomolecular recognition element can be achieved by the change in the propagation length. In SPR sensors, excitation of the SPP can occur if the electric field vector of the light is parallel to the metal surface and the momentum between light and the SPP can be matched. These can be achieved by means of prism coupling, grating coupling, fibre coupling and waveguide coupling [20–30], which have been described in section 2.2. In these cases, SPP biosensors can be classified as angle, wavelength, intensity, phase or polarization modulation-based sensors.

Traditional SPP biosensors work on the principle of prism coupling by altering the incidence angle to match the momentum. In contrast, SPP biosensors by fibre and waveguide incorporated grating structures have received increasing attention due to their high sensitivity. Nemova and Kashyap proposed a new SPP sensor with a fibre Bragg grating (FBG) imprinted into the fibre core [86], wherein the SPP excitation is based on resonance coupling of the fundamental fibre core mode to the counterpropagating SPP by means of the Bragg grating. In particular, the FBG exhibits highly efficient excitation of SPPs due to two main conditions: one is phase matching between the propagation constant of the fibre core mode and the SPP propagation constant provided by the properly designed period of the FBG for the predetermined wavelength of interest, and the other large coupling constant of the fibre core mode coupled to the SPP by a proper design of the fibre and the grating parameters. Moreover, the grating length and amplitude of refractive index modulation can be used for optimizing the grating reflectivity and the grating period, and the metal layer thickness can be used for controlling the sensor sensitivity. As a result, a measurement resolution of 1 part in 10^6 can be achieved for a change in refractive index of the surrounding material. The FBG can be applied to a planar waveguide biosensor without loss of generality. In addition, a side-polished fibre grating sensor for sensing ambient refractive index using 'pure' SPP excitation was presented [87]. The long-period grating based sensor is about 5–20 times more sensitive to the change in ambient refractive index and requires much shorter grating lengths for a given sensitivity than the one based on FBG, and maximum sensitivity can be obtained at an optimum value of metal thickness. On the other hand, waveguide Bragg gratings have been widely used in biosensors [88]. A waveguide SPP sensor with a UV-written Bragg grating was theoretically investigated using the perturbation method and Floquet mode formalism [89]. These methods are very important to both understanding sensor behaviour and development of waveguide grating SPP sensors. Moreover, integrated optical waveguide SPR sensors exhibit a promising candidate for the development of multichannel sensing devices on one chip with the potential for efficient referencing and multicomponent sensor analysis of complex samples [27]. A theoretical model of an integrated planar SPP sensor was presented. The main principle of the sensor operation is based on the high-efficiency energy transfer between the guided mode propagating in the waveguide layer separated by a buffer from the metal layer supporting the 'pure' SPP [90]. Furthermore, a simple integrated scheme for a SPP planar sensor was reported [91]. The sensors are free from any moving parts with a long-period corrugated metal grating engraved on the surface of the metal layer in contact with sensed medium. The long-period grating imprinted in the waveguide layer and buffer permit a dramatic enhancement in the sensitivity of the sensor in comparison with the short period grating used for SPP excitation. Recently, Holmes *et al* reported a planar-integrated SPP sensor based on the grating-matched coupling between a core waveguide mode and a set of hybrid SPP-dielectric modes of a much wider integrated structure. The sensitivity in the planar-integrated sensor is comparable to fibre-based SPP sensors but with the advantages of planar integration and microfluidic adaptation. Moreover, the spectral response of the sensor exhibits anomalous SPP effects, including a distinctly different response between orthogonal polarizations and a SPP-associated high loss region dependent on the refractive index of the analyte. Design of the planar waveguide sensor permits denser integration, miniaturization and microfluidic possibilities [92].

It is noted that noble metal nanoparticles can also act as transducers that convert small changes in the local refractive index into SPR peak shifts. The local refractive index increases when organic molecules bind to nanoparticles, which gives rise to the redshift of the SPR peak. For

example, SPR peak shift can be used for ultrasensitive quantification of proteins [93]. Concentrations of amyloid-derived diffusible ligands (ADDLs) were measured by an SPP peak-shift assay; a neurotoxin that was thought to be important in the pathology of Alzheimer's disease at concentrations down to 100fM [119]. Similarly elevated levels of ADDLs were observed in a population of 15 Alzheimer's patients and 15 ageing controls using a 'bio-barcode' assay that used SPP nanoparticle labels [94]. Detection of desirable biological molecules could be accomplished using SPP coupling between noble metal nanoparticles. Rosi and Mirkin reported a strong SPR peak redshift upon aggregation in the presence of a complementary nucleotide (nanostructured plasmonic sensors) using oligonucleotide-functionalized gold nanoparticles [95]. The colour change results from particle–particle SPP coupling as well as aggregate scattering, and they used oligonucleotide-functionalized gold nanoparticles to determine the relative binding strengths of a variety of duplex and triplex DNA-binding molecules [96, 97].

SPP biosensors can achieve an extremely small detection limit exceeding 10^{-5} refractive-index units (RIU) due to the SPP coupling effects. To improve the sensitivity for detection of small analytes further, recently, Kabashin, Zayats and co-workers have proposed an improvement in biosensor by using a SPP metamaterial that is capable of supporting a guided mode in a noble metal nanorod layer [98]. They connected the prism-based coupling block with a flow cell to allow access of the liquid to the nanorod assembly. Aqueous solutions of glycerine of different concentrations were then pumped through the cell to provide minute changes of the bulk refractive index of the nanorod surroundings. Figure 17 shows that the metamaterial works similarly to a conventional SPP-based sensor; a redshift of the resonance peak in response to an increase in the refractive index can be observed. Furthermore, a change in the refractive index by 10^{-4} RIU causes a shift of the resonance by 3.2 nm even without any optimization of the structure. The corresponding minimum estimation of sensitivity of 32 000 nm/RIU exceeds the sensitivity of localized plasmon-based schemes by two orders of magnitude. The sensitivity of a guided wave offered by the nanorod metamaterial also exceeds the relevant parameter for commercial SPP-based sensors using spectral interrogation. On the other hand, an advantage of the metamaterial-based sensor consists of the essentially discontinuous porous nanotexture of the nanorod matrix, which enables the implementation of new sensing geometries and strategies, not feasible with conventional film-based SPR. Indeed, by functionalizing the nanorods and immobilizing a receptor on their surface, one can follow the binding of a selective analyte with the receptor inside the nanorod matrix. The considerably increased surface area given by the nanoporous texture of the metamaterial significantly increases the amount of biomaterial that can be incorporated into the matrix within the available probe depth, maximizing the biological sensitivity of the system. Furthermore, the distance between the nanorods can be selected to match the size of biological species of interest, giving access to a further size selectivity option that is important for many tasks in immunoassays and virus and protein detection.

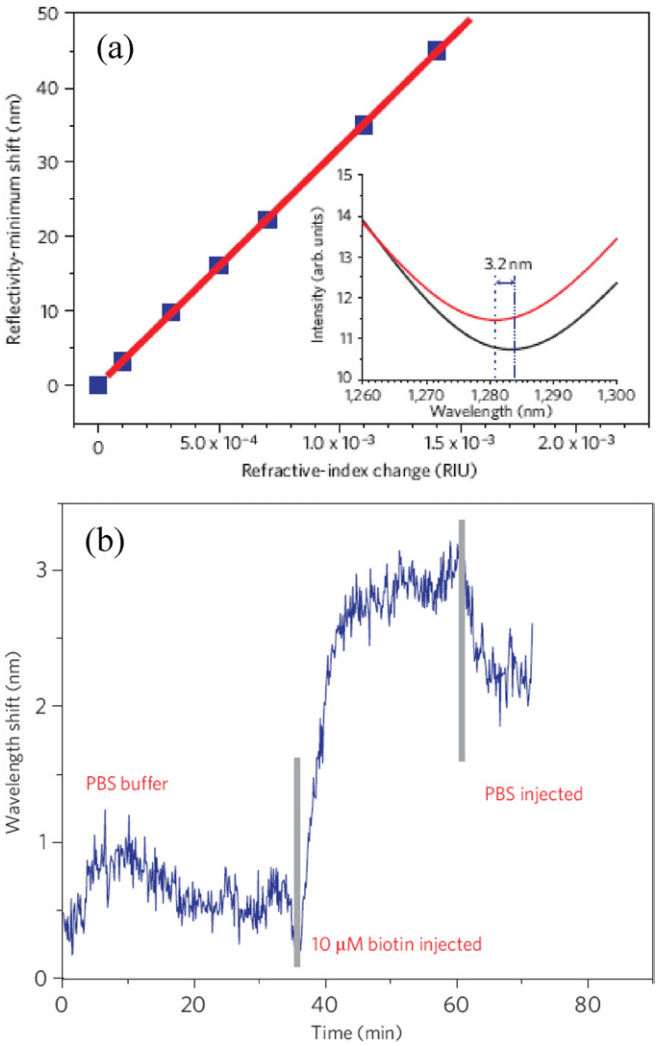

Figure 17. Nanorod-based sensor calibration and observation of the test binding reaction. (*a*) Calibration curve for the metamaterial-based sensor under the step-like changes of the refractive index of the environment using different glycerine–water solutions. The measurements were carried out at a wavelength of 1230 nm. Inset: reflectivity spectrum modifications with the changes of the refractive index by 10^{-4} RIU. (*b*) Response of the metamaterial-based biosensor to the reaction of biotin–streptavidin binding.

4. Conclusions

This paper provides a comprehensive overview of progress in current research in SPPs. SPPs are surface electromagnetic waves that propagate along the interface between a metal and a dielectric material. Excitation of SPPs can overcome the diffraction limit to about one-half of the optical wavelength and offer a promising approach to control and manipulation of light on subwavelength and nanometre scales. The interaction between the electromagnetic field and the SPP results in an increase in SPP momentum corresponding to that of the free space based on the nonlinear dispersion relation of SPPs. Moreover, the momentum of photon and SPP can be matched by using light tunnelling in the total internal reflection geometry or diffraction effects. In addition, the propagation length of SPP is dependent mainly on the dielectric constant

of the metal and the incident wavelength, and the propagation length can increase by decreasing the loss (e.g. selecting a low-loss metal, such as silver, with a small imaginary component of the dielectric constant) or increasing the incident wavelength.

SPPs have received considerable attention and interest from physicists, chemists, materials scientists and biologists. A large number of novel and potential applications of SPPs have been performed owing to their unique characteristics. For instance, noble metal nanoparticles, nanowires and nanochannels can be worked as SPP waveguides, and SPPs can propagate along the interface containing noble metal by design of those special structures. By constructing noble metal periodical nanostructures, subwavelength metal–dielectric cavities or nanoantennas, SPPs can be focused on very small spots on nanometre scales and designed as nanosources. Due to the enhanced local electric fields of SPPs, noble metal nanostructures can be used for the probes of scanning near-field optical microscopes, which perform super-resolution and high sensitivity behaviour. In this case, we can realize manipulation of the photons in near-field space beyond the diffraction limit. One of the most interesting applications of SPPs is surface-enhanced Raman scattering (SERS). Owing to the electromagnetic field enhancement from coupling to SPPs, Raman signals of adsorbed molecules can be amplified remarkably. As a result, probing of single molecule can be achieved, and noble metal nanostructures working as SERS substrates will also exhibit a great potential in trace detections of persistent organic pollutants. Moreover, SPPs can be used for near-field optical data storage with super-high information density beyond 1 Tbit cm^{-3}; especially, noble metal nanorods with longitudinal SPP resonance can realize five-dimensional optical recording with synchronous integration of wavelength, polarization and spatial dimensions. Noble metal nanostructured thin films have the potential to confine and guide incident light into a subwavelength thickness absorber layer. Due to excitation of SPPs, the photovoltaic conversion efficiency of solar cells can be enhanced notably by incorporation of the metal nanostructures. Noble metal nanostructures can serve as chemical sensors and biosensors based upon the environmental medium dependence of the dielectric constant change, and SPP biosensors can obtain an extremely small detection limit exceeding 10^{-5} refractive-index units (RIU) due to the SPP coupling effects.

SPPs constitute a main part of nanophotonics. Control and manipulation of photons using SPPs on nanometre scales exhibit significant advantages and challenges in nanophotonic devices with very small elements, high performance, high efficiency and high stability. All-optical integration devices based on SPP nanoscience and nanotechnology may be realized by optimal design of materials. In particular, SPPs open a new and promising way to the fields involving environment, energy, biology, chemistry, medicine and health.

Acknowledgments

The authors are grateful to all their colleagues who in one way or another contributed to the review article. This work is supported by the National Natural Science Foundation of China (Grant No 10804112), the National Basic Research Program of China (973 Program, Grant No 2012CB932303) and the Knowledge Innovation Program of the Chinese Academy of Sciences (Grant No 074N4H1121).

References

[1] Wood R W 1902 *Phil. Mag.* **4** 396
[2] Maxwell Garnett J C 1904 *Phil. Trans. R. Soc. Lond.* **203** 385
[3] Mie G 1908 *Ann. Phys.* **25** 377
[4] Pines D 1956 *Rev. Mod. Phys.* **28** 184
[5] Fano U 1956 *Phys. Rev.* **103** 1202
[6] Ritchie R H 1957 *Phys. Rev.* **106** 874
[7] Ritchie R H, Arakawa E T, Cowan J J and Hamm R N 1968 *Phys. Rev. Lett.* **21** 1530
[8] Otto A 1968 *Z. Phys.* **216** 398
[9] Kretschmann E and Raether H 1968 *Z. Naturf.* A **23** 2135
[10] Kreibig U and Zacharias P 1970 *Z. Phys.* **231** 128
[11] Cunningham S L, Maradudin A A and Wallis R F 1974 *Phys. Rev.* B **10** 3342
[12] Barnes W L, Dereux A and Ebbesen T W 2003 *Nature* **424** 824
[13] Specht M, Pedarnig J D, Heckl W M and Hänsch T W 1992 *Phys. Rev. Lett.* **68** 476
[14] Ashino M and Ohtsu M 1998 *Appl. Phys. Lett.* **72** 1299
[15] Zijlstra P, Chon J W M and Gu M 2009 *Nature* **459** 410
[16] Oldenburg S J, Genick C C, Clark K A and Schultz D A 2002 *Anal. Biochem.* **309** 109
[17] Nie S M and Emory S R 1997 *Science* **275** 1102
[18] Palik E D 1985 *Handbook of Optical Constants of Solids* (New York: Academic) p 275
[19] Pitarke J M, Silkin V M, Chulkov E V and Echenique P M 2007 *Rep. Prog. Phys.* **70** 1
[20] Zayats A V, Smolyaninov I I and Maradudin A A 2005 *Phys. Rep.* **408** 131
[21] Sarid D 1981 *Phys. Rev. Lett.* **47** 1927
[22] Berini P 2009 *Adv. Opt. Photon.* **1** 484
[23] Zayats A V and Smolyaninov I I 2003 *J. Opt.* A **5** S16
[24] Berini P, Charbonneau R, Lahoud N and Mattiussi G 2005 *J. Appl. Phys.* **98** 043109
[25] Barnes W L 2006 *J. Opt.* A **8** S87
[26] Berini P and De Leon I 2012 *Nature Photon.* **6** 16
[27] Homola J, Yee S S and Gauglitz G 1999 *Sensors Actuators* B **54** 3
[28] Abdulhalim I, Zourob M and Lakhtakia A 2008 *Electromagnetics* **28** 214
[29] Kashyap R and Nemova G 2009 *J. Sensors* **2009** 1
[30] Sharma A K, Jha R and Gupta B D 2007 *IEEE Sensors J.* **7** 1118
[31] Bozhevolnyi S I, Erland J, Leosson K, Skovgaard P M W and Hvam J M 2001 *Phys. Rev. Lett.* **86** 3008
[32] Quinten M, Leitner A, Krenn J R and Aussenegg F R 1998 *Opt. Lett.* **23** 1331
[33] Maier S A, Kik P G, Atwater H A, Meltzer S, Harel E, Koel B and Requicha A G 2003 *Nature Mater.* **2** 229
[34] Weeber J C, Dereux A, Girard C, Krenn J R and Goudonnet J P 1999 *Phys. Rev.* B **60** 9061
[35] Bozhevolnyi S I, Erland J, Leosson K, Skovgaard P M W and Hvam J M 2001 *Phys. Rev. Lett.* **86** 3008
[36] Oulton R F, Sorger V J, Genov D A, Pile D F P and Zhang X 2008 *Nature Photon.* **2** 496
[37] Pyayt A L, Wiley B, Xia Y N, Chen A and Dalton L 2008 *Nature Nanotechnol.* **3** 660
[38] Bozhevolnyi S I, Volkov V S, Devaux E and Ebbesen T W 2005 *Phys. Rev. Lett.* **95** 046802
[39] Bozhevolnyi S I, Volkov V S, Devaux E, Laluet J Y and Ebbesen T W 2006 *Nature* **440** 508

[40] Nagpal P, Lindquist N C, Oh S H and Norris D J 2009 *Science* **325** 594
[41] Lezec H J, Degiron A, Devaux E, Linke R A, Martin-Moreno L, Garcia-Vidal F J and Ebbesen T W 2002 *Science* **297** 820
[42] Lerosey G, Pile D F P, Matheu P, Bartal G and Zhang X 2009 *Nano Lett.* **9** 327
[43] Koenderink A F 2009 *Nano Lett.* **9** 4228
[44] Oulton R F, Sorger V J, Zentgraf T, Ma R M, Gladden C, Dai L, Bartal G and Zhang X 2009 *Nature* **461** 629
[45] Fang Z Y, Peng Q A, Song W T, Hao F H, Wang J, Nordlander P and Zhu X 2011 *Nano Lett.* **11** 893
[46] Kim Y K, Lundquist P M, Helfrich J A, Mikrut J M, Wong G K, Auvil P R and Ketterson J B 1995 *Appl. Phys. Lett.* **66** 3407
[47] Kryukov A E, Kim Y K and Ketterson J B 1997 *J. Appl. Phys.* **82** 5411
[48] Melville D O S, Blaikie R J and Wolf C R 2004 *Appl. Phys. Lett.* **84** 4403
[49] Pendry J B 2000 *Phys. Rev. Lett.* **85** 3966
[50] Kawata S, Inouye Y and Verma P 2009 *Nature Photon.* **3** 388
[51] Fang N, Lee H, Sun C and Zhang X 2005 *Science* **308** 534
[52] Lee H, Xiong Y, Fang N, Srituravanich W, Durant S, Ambati M, Sun C and Zhang X 2005 *New J. Phys.* **7** 255
[53] Achermann M, Shuford K L, Schatz G C, Dahanayaka D H, Bumm L A and Klimov V I 2007 *Opt. Lett.* **32** 2254
[54] Kim S, Jin J H, Kim Y J, Park I Y, Kim Y and Kim S W 2008 *Nature* **453** 757
[55] Schnell M, Garcia-Etxarri A, Huber A J, Crozier K, Aizpurua J and Hillenbrand R 2009 *Nature Photon.* **3** 287
[56] Kosako T, Kadoya Y and Hofmann H F 2010 *Nature Photon.* **4** 312
[57] Kosako T, Hofmann H F and Kadoya Y 2009 *Conf. on Lasers and Electro-Optics and Quantum electronics and Laser Science Conf. (CLEO/QELS 2009) (Baltimore, MD)* vol 2, p 1891
[58] Hofmann H F, Kosako T and Kadoya Y 2007 *New J. Phys.* **9** 217
[59] Li J J, Salandrino A and Engheta N 2009 *Phys. Rev.* B **79** 195104
[60] Li J J, Salandrino A and Engheta N 2007 *Phys. Rev.* B **76** 245403
[61] Taminiau T H, Stefani F D and van Hulst N F 2008 *Opt. Express* **16** 10858
[62] Curto A G and Van Hulst N F 2009 *Master in Photonics* Universidad de Barcelona
[63] Smythe E J, Dickey M D, Bao J, Whitesides G M and Capasso F 2009 *Nano Lett.* **9** 1132
[64] Kneipp K, Wang Y, Kneipp H, Perelman L T, Itzkan I, Dasari R and Feld M S 1997 *Phys. Rev. Lett.* **78** 1667
[65] Michaels A M, Nirmal M and Brus L E 1999 *J. Am. Chem. Soc.* **121** 9932
[66] Kneipp K, Moskovits M and Kneipp H (ed) 2006 *Surface-Enhanced Raman Scattering: Physics and Applications* (Berlin: Springer)
[67] Hao E and Schatz G C 2004 *J. Chem. Phys.* **120** 357
[68] Fang Y, Seong N H and Dlott D D 2008 *Science* **321** 388
[69] Xu W, Zhang J X, Zhang L D, Hu X Y and Cao X L 2009 *J. Nanosci. Nanotechnol.* **9** 4812
[70] Xu W, Zhang L D, Zhang J X, Hu X Y and Sun L 2009 *Appl. Surf. Sci.* **255** 6612
[71] Fang Y R, Wei H, Hao F, Nordlander P and Xu H X 2009 *Nano Lett.* **9** 2049
[72] Gopinath A, Boriskina S V, Premasiri W R, Ziegler L, Reinhard B M and Negro L D 2009 *Nano Lett.* **9** 3922
[73] Hermann C, Kosobukin V A, Lampel G, Peretti J, Safarov V I and Bertrand P 2001 *Phys. Rev.* B **64** 235422
[74] Mansuripur M, Zakharian A R, Lesuffleur A, Oh S H, Jones R J, Lindquist N C, Im H, Kobyakov A and Moloney J V 2009 *Opt. Express* **17** 14001
[75] O'Connor D and Zayats A V 2010 *Nature Nanotechnol.* **5** 482
[76] Stenzel O, Stendal A, Voigtsberger K and Vonborczyskowski C 1995 *Sol. Energy Mater. Sol. Cells* **37** 337
[77] Westphalen M, Kreibig U, Rostalski J, Luth H and Meissner D 2000 *Sol. Energy Mater. Sol. Cells* **61** 97
[78] Ferry V E, Sweatlock L A, Pacifici D and Atwater H A 2008 *Nano Lett.* **8** 4391
[79] Brown M D, Suteewong T, Kumar R S S, D'Innocenzo V, Petrozza A, Lee M M, Wiesner U and Snaith H J 2011 *Nano Lett.* **11** 438
[80] Raschke G *et al* 2004 *Nano Lett.* **4** 1853
[81] Daniel M C and Astruc D 2004 *Chem. Rev.* **104** 293
[82] Moores A, Goettmann F, Sanchez C and Le Floch P 2004 *Chem. Commun.* 2842
[83] Mezailles N, Mathey F and Le Floch P 2001 *Prog. Inorg. Chem.* **49** 455
[84] Goettmann F, Moores A, Boissière C, Le Floch P and Sanchez C 2005 *Small* **1** 636
[85] Homola J 2003 *Anal. Bioanal. Chem.* **377** 528
[86] Nemova G and Kashyap R 2006 *Opt. Lett.* **31** 2118
[87] Tripathi S M, Kumar A, Marin E and Meunier J P 2008 *J. Lightwave Technol.* **26** 1980
[88] Usbeck K, Ecke W, Andreev A, Hagemann V, Mueller R and Willisch R 1998 *Proc. SPIE* **3483** 90
[89] ČtyrokÝ J, Abdelmalek F, Ecke W and Usbeck K 1999 *Opt. Quantum Electron.* **31** 927
[90] Nemova G and Kashyap R 2007 *Opt. Commun.* **275** 76
[91] Nemova G and Kashyap R 2008 *Opt. Commun.* **281** 1522
[92] Holmes C, Daly K R, Sparrow I J G, Gates J C, D'Alessandro G and Smith P G R 2011 *IEEE Photon. J.* **3** 777–88
[93] Anker J N, Hall W P, Lyandres O, Shah N C, Zhao J and Van Duyne R P 2008 *Nature Mater.* **7** 442
[94] Georganopoulou D G, Chang L, Nam J M, Thaxton C S, Mufson E J, Klein W L and Mirkin C A 2005 *Proc. Natl Acad. Sci. USA* **102** 2273
[95] Rosi N L and Mirkin C A 2005 *Chem. Rev.* **105** 1547
[96] Han M S, Lytton-Jean A K R and Mirkin C A 2006 *J. Am. Chem. Soc.* **128** 4954
[97] Han M S, Lytton-Jean A K R, Oh B K, Heo J and Mirkin C A 2006 *Angew. Chem. Int. Edn* **45** 1807
[98] Kabashin A V, Evans P, Pastkovsky S, Hendren W, Wurtz G A, Atkinson R, Pollard R, Podolskiy V A and Zayats A V 2009 *Nature Mater.* **8** 867
[99] Altug H, Englund D and Vuckovic J 2006 *Nature Phys.* **2** 484
[100] Hill M T, Oei Y S, Smalbrugge B, Zhu Y C, De Vries T, van Veldhoven P J, van Otten F W M , Eijkemans T J, Turkiewicz J P, De Waardt H, Geluk E J, Kwon S H, Lee Y H, Nötzel R and Smit M K 2007 *Nature Photon.* **1** 589
[101] Johnson J C, Choi H J, Knutsen K P, Schaller R D, Yang P D and Saykally R J 2002 *Nature Mater.* **1** 106
[102] Duan X F, Huang Y, Agarwal R and Lieber C M 2003 *Nature* **421** 241
[103] Muhlschlegel P, Eisler H J, Martin O J F, Hecht B and Pohl D W 2005 *Science* **308** 1607
[104] Novotny L 2007 *Phys. Rev. Lett.* **98** 266802
[105] Fleischm M, Hendra P J and McQuilla A J 1974 *Chem. Phys. Lett.* **26** 163
[106] Jeanmaire D L and Van Duyne R P 1977 *J. Electroanal. Chem.* **84** 1
[107] Albrecht M G and Creighton J A 1977 *J. Am. Chem. Soc.* **99** 5215

[108] Moskovits M 1978 *J. Chem. Phys.* **69** 4159
[109] Ditlbacher H, Krenn J R, Lamprecht B, Leitner A and Aussenegg F R 2000 *Opt. Lett.* **25** 563
[110] Pham H H, Gourevich I, Oh J K, Jonkman J E N and Kumacheva E 2004 *Adv. Mater.* **16** 516
[111] Alasfar S, Ishikawa M, Kawata Y, Egami C, Sugihara O, Okamoto N, Tsuchimori M and Watanabe O 1999 *Appl. Opt.* **38** 6201
[112] Wilson O, Wilson G J and Mulvaney P 2002 *Adv. Mater.* **14** 1000
[113] Strickler J and Webb W 1991 *Opt. Lett.* **16** 1780
[114] Cumpston B H *et al* 1999 *Nature* **398** 51
[115] Zhang J X, Zhang L D, Ye C H, Chang M, Yan Y G and Lu Q F 2004 *Chem. Phys. Lett.* **400** 158
[116] Zhang J X, Yan Y G, Cao X L and Zhang L D 2006 *Appl. Opt.* **45** 297
[117] Snaith H J and Schmidt-Mende L 2007 *Adv. Mater.* **19** 3187
[118] Ellis A B and Walt D R 2000 *Chem. Rev.* **100** 2477
[119] Hardy J and Selkoe D J 2002 *Science* **297** 353